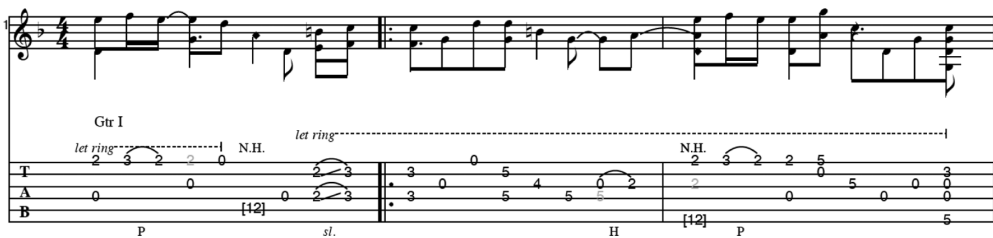


10

Dansgaard-Oeschger Events



Flip-flops under icy conditions.

CADGAD, Ragamuffin, Michael Hedges

One of the main breakthroughs in climate research over the past decades has been the reconstruction of past temperatures from ice cores. A surprising result was the discovery of millennial time-scale variability during the last glacial period. In this chapter, stochastic dynamical systems theory is used to understand the characteristics of this millennial climate variability.

10.1 Phenomena

At the moment, analyses from ice cores drilled on Greenland (Andersen et al., 2004) and on Antarctica (EPICA, 2006) are available. From the Greenland ice cores, the local temperature could be determined down to about 100-kyr BP. From the European Project for Ice Coring in Antarctica (EPICA) core data, temperatures and greenhouse gas concentrations over the last 800,000 years could be reconstructed.

Water in ice cores contains two isotopes of oxygen, ^{18}O and ^{16}O . The normalised isotope ratio $\delta^{18}\text{O}$ is calculated as a deviation from a reference sample as

$$\delta^{18}\text{O} = \frac{\left(\frac{^{18}\text{O}}{^{16}\text{O}}\right)_{\text{sample}} - \left(\frac{^{18}\text{O}}{^{16}\text{O}}\right)_{\text{reference}}}{\left(\frac{^{18}\text{O}}{^{16}\text{O}}\right)_{\text{reference}}}, \quad (10.1)$$

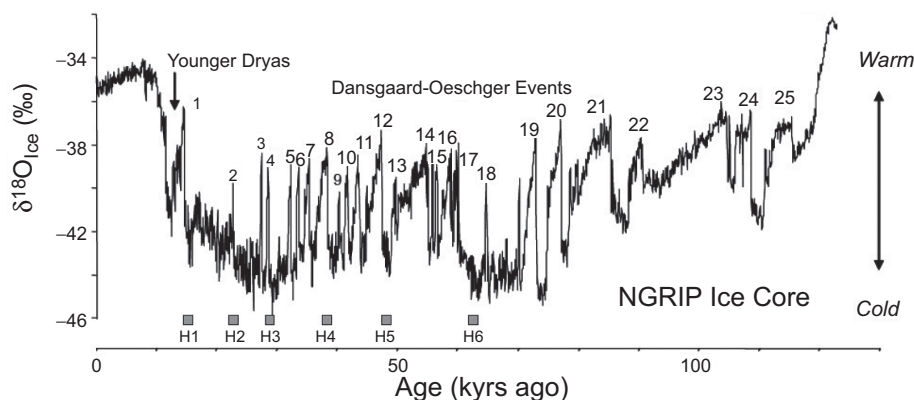


Figure 10.1 Plot of the $\delta^{18}\text{O}$ data from the NGRIP ice core record (Andersen et al., 2004). The numbers refer to the interstadials (warm periods), the occurrence of the Heinrich events is shown by the labels H_1 to H_6 and the Younger Dryas is indicated by an arrow (figure from Clement and Peterson, 2008).

where the reference sample is ‘standard mean’ ocean water. The isotope ^{16}O is lighter than ^{18}O so that water containing ^{16}O is preferentially evaporated and a temperature-dependent fractionation occurs. Changes in $\delta^{18}\text{O}$ reflect the combined effect of changes in global ice volume and temperature at the time of deposition of the sampled material. During very cold conditions, global ice volume is relatively large and hence sea level is low, which enriches water in the ocean with ^{18}O . Also because of the colder temperatures, more ^{18}O remains in the ocean and less ^{18}O becomes locked in the ice. Hence the ratio $\delta^{18}\text{O}$ in ice cores will decrease (become more negative) under colder conditions.

An example of a $\delta^{18}\text{O}$ record from the North Greenland Ice Core Project (NGRIP) ice core data is provided in Fig 10.1. The record spans the last 123,000 years and reveals changes between relatively cold periods (so-called stadials) and warm periods (so-called interstadials). Relatively rapid climatic shifts occurred during the period 70–10 kyr BP, with peak-to-peak temperature changes of about 10°C . These changes are generally referred to as Dansgaard-Oeschger (hereafter D-O) events. Fig. 10.1 shows that most D-O events are characterised by a rapid warming transition and a slow cooling phase.

There has been an extensive discussion on the dominant time scale of the D-O events (Wunsch, 2000). After careful analysis of the GISP2 (Stuiver and Grootes, 2000) record, Schulz (2002) concluded that between 46 and 13 kyr BP, the onset of D-O events was paced by a fundamental period of $\sim 1,470$ years. Before 50 kyr BP, the presence of such a dominant period is unclear due to dating uncertainties in the ice core record.

Bond et al. (1997) have shown that individual D-O events are apparently clustered to form a longer sawtooth-shaped cycle with a time scale of about 10,000 years; this

is sometimes referred to as the Bond cycle. In the ice core records, discrete layers of ice-rafted debris have also been found, which were deposited during the coldest phases of several D-O events. These so-called Heinrich events (H_1 – H_6 in Fig 10.1) are interpreted as large bursts of freshwater into the North Atlantic due to massive iceberg releases through the Hudson Strait. The last rapid shift in Greenland temperatures occurred as a period of significant cooling between 12,500 and 11,500 years ago. The resulting stadial is referred to as the Younger Dryas, during which the apparent warming trend from the Last Glacial to the Holocene was delayed for approximately 1,000 years (Fig 10.1). The Younger Dryas period ends with a rapid shift to warmer temperatures into the beginning of the Holocene.

There are many indications from proxy data that there have been large-scale reorganisations of both the atmosphere and ocean associated with D-O events, and a recent review is provided in Clement and Peterson (2008). In the subpolar North Atlantic, D-O events were matched with corresponding sea-surface temperature changes of at least 5°C. Of special interest is that the temperature anomalies on Antarctica are about 180° out of phase with those on Greenland.

The behaviour of the climate system on millennial time scales during the last glacial period is highly interesting for an understanding of feedbacks among the ocean, atmosphere and cryosphere. A theory of D-O events will have to explain at least the processes controlling:

- (i) the dominant $\sim 1,500$ -year time scale of the variability;
- (ii) the asymmetric character of the transition with a rapid warming and a relatively slow cooling phase; and
- (iii) the phase difference between the temperature in the northern and southern polar regions.

Finally, the theory should provide an explanation for why there are no D-O events observed in the Holocene and a consistent causal connection among D-O events, the Bond cycle and the Heinrich events. As discussed in Clement and Peterson (2008), several different views have been proposed to explain the millennial climate variability during the last glacial period. Leading theories involve changes in the global ocean circulation and stochastic resonance. In this chapter, we start with the basic ingredients of the present-day ocean circulation, then discuss transitions in ocean circulation patterns and, finally, look at the effect of noise on these transitions.

10.2 The meridional overturning circulation

On the large scale, the ocean circulation is driven by momentum fluxes (wind stress) and affected by fluxes of heat and freshwater at the ocean-atmosphere interface. The

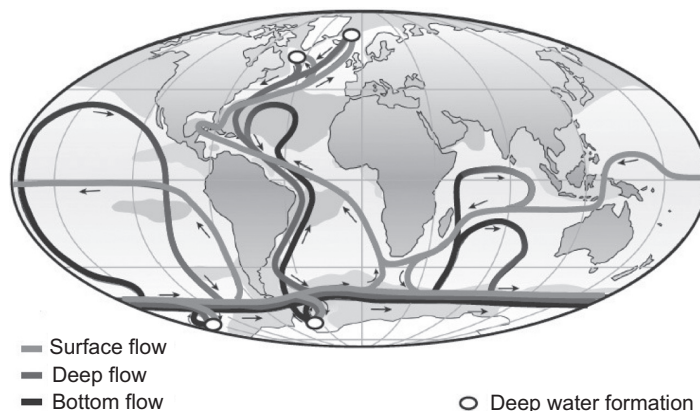


Figure 10.2 Strongly simplified sketch of the global ocean circulation. In the North Atlantic, warm and saline waters flow northward into the deep water formation areas (indicated by small circles). Bottom water is also formed in the Southern Ocean (figure modified Kuhlbrodt et al., 2007).

latter fluxes change the surface density of the ocean water, and through mixing and advection, density differences are propagated horizontally and vertically.

An illustration of the global ocean circulation is provided in Fig. 10.2. In the North Atlantic, the Gulf Stream transports relatively warm and saline waters northwards. The heat is quickly taken up by the atmosphere, making the water denser. When there is strong cooling in winter, the water column becomes unstably stratified in certain areas (e.g., the Greenland Sea and the Labrador Sea), resulting in strong convection. The net result of this is the formation of a water mass called North Atlantic Deep Water (NADW), which overflows the various ridges that are present in the topography and enters the Atlantic basin.

The NADW flows southwards at mid-depth in the Atlantic, enters the Southern Ocean and from there reaches the other ocean basins. Through upwelling in the Atlantic, Southern, Pacific and Indian Oceans, water is slowly brought back to the surface, and the mass balance is closed by transport back to the sinking areas in the North Atlantic. In the Southern Ocean, bottom water is formed (the Antarctic Bottom Water, AABW), which has a higher density than NADW and therefore appears in the abyssal Atlantic. In the North Pacific, no deep water is produced. The deep water formation at high latitudes, the upwelling at lower latitudes and in the Southern Ocean and the horizontal currents together form the global ocean circulation.

A crucial component of the global ocean circulation is the meridional overturning circulation (MOC), which is the zonally integrated volume transport. The MOC is strongly coupled to meridional heat transport. There are no observations available to reconstruct the pattern of the MOC, but its strength at 26°N in the Atlantic is now routinely monitored by the RAPID-MOCHA array (Cunningham et al., 2007). The

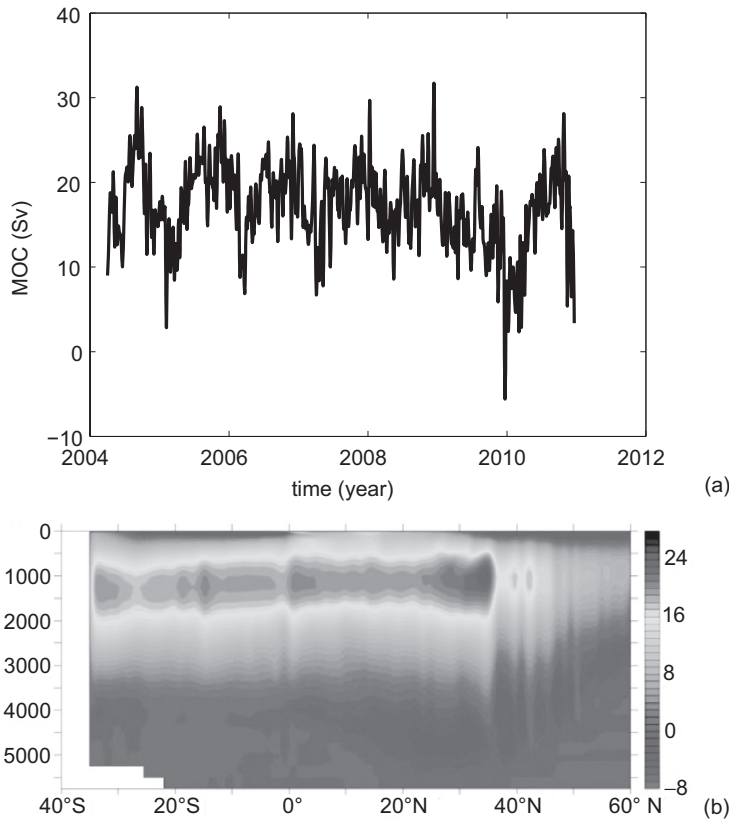


Figure 10.3 (a) Volume transports of the Atlantic MOC at 26°N as measured by the RAPID-MOCHA array (Cunningham et al., 2007). Data are taken from <http://www.noc.soton.ac.uk/rapidmoc/>. (b) Contour plot of the 10-year mean MOC (contours in Sv) in the Atlantic from the control simulation (C-MIXED) with the POP 0.1° high-resolution model. The depth on the vertical axis is in meters (figure from Weijer et al., 2012). (See Colour Plate.)

currently available time series of the MOC strength is shown in Fig. 10.3a, indicating the large amplitude variability. The pattern of the MOC can be determined from numerical ocean models, and a typical pattern of the Atlantic MOC from a high-resolution ocean model is plotted in Fig. 10.3b. At 26°N the heat transport associated with the Atlantic MOC is estimated to be 1.2 PW (Johns et al., 2011).

In a glacial period, with different insolation and CO₂ levels, of course the forcing of the ocean circulation differed markedly. Proxy data indicate that the NADW cell was weaker during glacial times, in particular during the Last Glacial Maximum, and there was enhanced intrusion of AABW into the Atlantic basin (Clement and Peterson, 2008). These proxy data hence imply that the glacial Atlantic MOC was likely weaker than today.

10.3 Sensitivity of the MOC: hysteresis

The North Atlantic experiences heat input and freshwater loss at low latitudes and heat loss and freshwater input at high latitudes. The surface freshwater flux and heat flux therefore have opposite effects on the meridional density gradient affecting the large-scale ocean circulation. This makes it interesting to investigate what happens when the relative importance of the two surface fluxes varies.

As already mentioned in Chapter 6, Stommel (1961) proposed a box model that can be used to study this problem in its simplest form. Under appropriate scaling (see Example 6.1), the dimensionless equations become

$$\frac{dT}{dt} = \eta_1 - T(1 + |T - S|), \quad (10.2a)$$

$$\frac{dS}{dt} = \eta_2 - S(\eta_3 + |T - S|). \quad (10.2b)$$

Here T and S monitor the dimensionless equatorial-to-pole temperature and salinity difference, $\Psi = T - S$ is the dimensionless MOC strength (positive when there is sinking in the northern box) and t indicates dimensionless time. The parameters η_1 and η_2 represent the strength of the thermal and freshwater forcing, respectively, and η_3 is the ratio of the thermal and freshwater surface restoring time scales (Example 6.1).

The bifurcation diagram for this model is shown (with the steady-state value $\bar{\Psi}$ plotted versus η_2) in Fig. 10.4a. For small η_2 , a unique steady state with $\bar{\Psi} > 0$ is reached for all initial states. This state is called the thermally dominated state or TH state (left panel in Fig. 10.4b). For large η_2 , again a unique steady state exists with $\bar{\Psi} < 0$, which is called the salinity dominated state or SA state (right panel in Fig. 10.4b). For values of η_2 up to the point L_1 , only the TH state is linearly stable, whereas for values beyond L_2 , only the SA state is linearly stable. On the branch that connects the solutions at L_1 and L_2 , the steady states are unstable. Between the points L_1 and L_2 , the TH and SA solutions coexist and are both linearly stable.

The multiple equilibria arise due to a positive feedback between the flow and the salt transport, called the salt-advection feedback (Walsh, 1985). The surface forcing salinifies and warms the low-latitude region, whereas it freshens and cools the high-latitude region. If the circulation strengthens, then more salt is transported poleward. This enhanced salt transport will increase further the density in high latitudes and, consequently, amplify the original perturbation of the circulation. The strengthening of the circulation also transports more heat northward; this will weaken the flow by lowering the density in high latitudes. This negative feedback is, however, weak, as the atmosphere strongly dampens surface temperature anomalies. On the contrary, ocean water salinity does not affect the freshwater flux at all.

Although the bifurcation diagram as in Fig. 10.4a is obtained from a relatively simple model, it turns out that this diagram is found in bifurcation studies using a

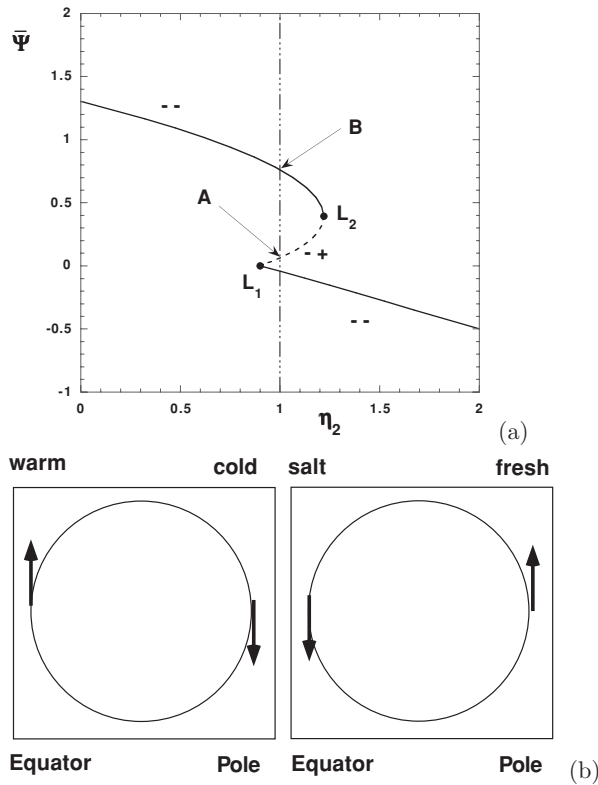


Figure 10.4 (a) Bifurcation diagram of the Stommel two-box model (10.2) for $\eta_1 = 3.0$ and $\eta_3 = 0.3$. (b) Patterns of the thermally driven (TH) MOC state (left panel) and the salinity driven (SA) MOC state (right panel).

hierarchy of two-dimensional and three-dimensional ocean models. For example, the bifurcation diagram found in the global ocean model of Dijkstra and Weijer (2005) is plotted in Fig. 10.5a. Here the strength of the Atlantic MOC (ψ) of each steady state is plotted versus the strength (γ_p in Sv) of a freshwater flux change in the northern North Atlantic. Again, a solid line style along the branch indicates that steady solutions are stable, whereas steady states are unstable on the dashed part of the branch. There are also two saddle-node bifurcations, indicated again by L_1 and L_2 , respectively, which separate the stable and unstable parts of the branch (Fig. 10.5b).

In many models such as EMICs and GCMs (cf. Section 6.1), however, the bifurcation diagrams cannot be directly computed. In this case, so-called quasi-equilibrium transient simulations are carried out, in which a parameter such as γ_p is changed very slowly in time (Fig. 10.5c); such simulations are usually referred to as ‘hosing experiments’ and are examples of fast-slow systems as discussed in Section 2.3.3. Starting at the reference solution for $\gamma_p = 0$, the upper solution branch in Fig. 10.5b is then followed until L_2 , where no nearby steady-state solution exists anymore. Hence the

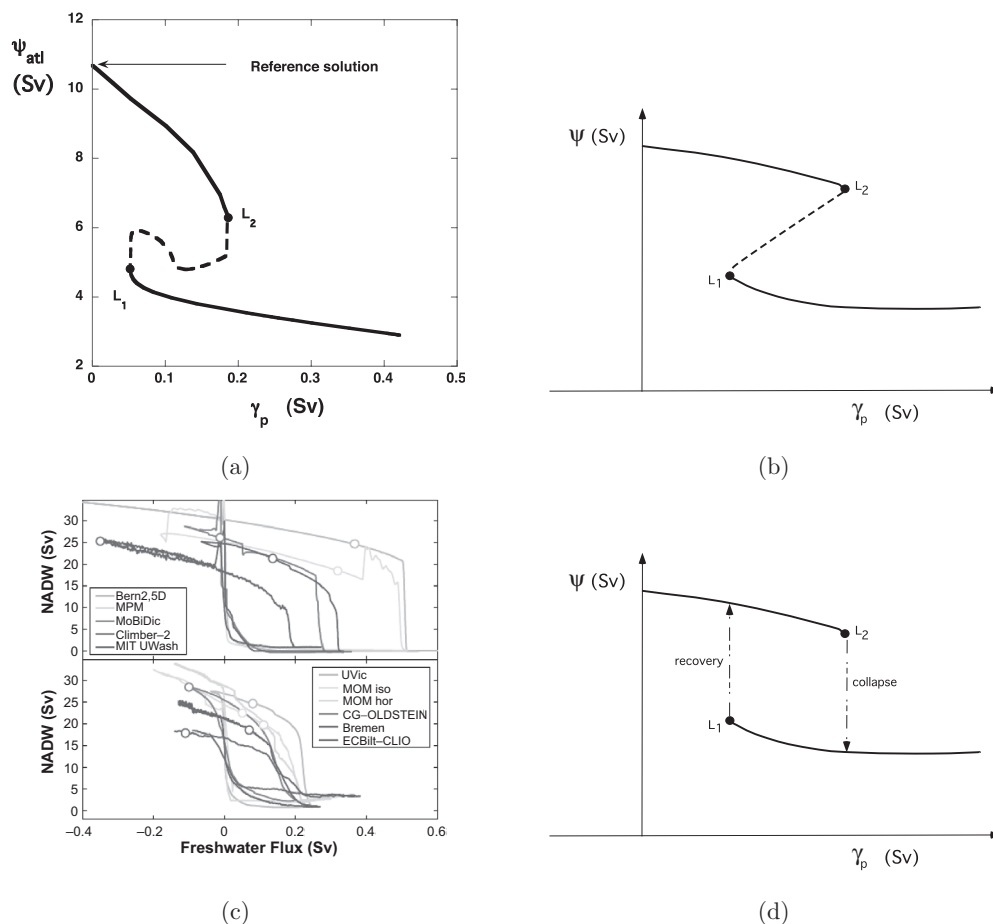


Figure 10.5 (a) Bifurcation diagram as found in the global ocean model in Dijkstra and Weijer (2005) with two saddle-node bifurcations labelled L_1 and L_2 . The parameter γ_p represents an additional freshwater flux in the northern North Atlantic. Solid parts of the branch indicate stable steady solutions, and steady states are unstable along the dashed part of the branch. (b) Sketch of this bifurcation diagram to compare with (d). (c) Typical hysteresis behaviour as found in a set of EMICs (Rahmstorf et al., 2005) when the freshwater flux is increased slowly in time from zero up to large values and back. On the vertical axis is a measure of the strength of the MOC. The curves are lined up with the recovery, and the equilibrium solutions obtained with zero freshwater perturbation are shown as open circles. (d) Sketch of the quasi-equilibrium simulations with γ_p . Near the saddle-node bifurcations in (a), the solution jumps from one stable steady state to another. The direction of these transient jumps is indicated with an arrow. (See Colour Plate.)

solution changes rapidly ('collapse' in Fig. 10.5d) to that on the lower branch and follows that branch with increasing γ_p . If from a large value of γ_p the solution is followed with decreasing γ_p , then the lower branch is followed down to γ_p at L_1 , where a transition ('recovery' in Fig. 10.5d) occurs to the solution on the upper branch.

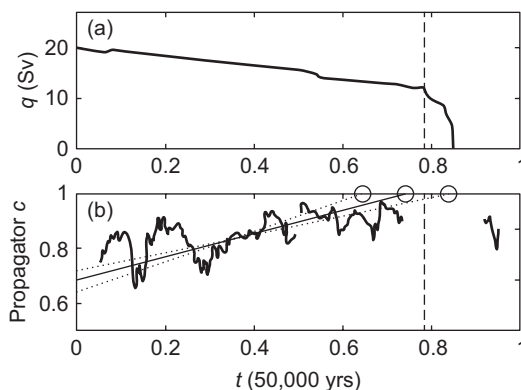


Figure 10.6 (a) Transport of the Atlantic meridional overturning and (b) AR(1) propagator c over time. Here c is obtained from a moving 10% time window. Although (a) shows artificially low variability, no early warning sign for a threshold behaviour is observable. The value of (b) is noisy but is much more informative on the approach to the critical transition (figure from Held and Kleinen [2004]).

Let the value of γ_p at L_i be indicated by γ_p^i ; the width of the hysteresis, say Δ_H , then is given by $\Delta_H = \gamma_p^2 - \gamma_p^1$. In typical ocean model studies, where γ_p is varied with about 0.01 Sv/1,000 years, one finds approximations of the value of Δ_H because the jumps are not really ‘vertical’ as in Fig. 10.5d; values of Δ_H are also strongly model dependent (Rahmstorf et al., 2005), as can be seen from Fig. 10.5c.

In Fig. 10.6, the degenerate fingerprinting technique (cf. Section 5.5.3) is applied to a time series from an EMIC to detect the saddle-node bifurcation L_2 . The freshwater input is slowly changing, decreasing the value of the meridional overturning transport q (Fig. 10.6a) over a period of 50,000 years. The value of the AR(1) coefficient c in (5.80) is obtained from a moving 10% window and shows an approach to unity as the transport of q rapidly decreases (Held and Kleinen, 2004).

Both the degenerate fingerprinting or autocorrelation function technique (ACF) and the detrended fluctuation analysis (DFA) were applied to similar simulations by another EMIC, and the results are summarized in Fig. 10.7. For this example, both indicators as well as the variance first increase when the saddle-node is approached, but the DFA and ACF do not show monotonic behaviour up to the critical point. Hence the signal from the indicators may in this case lead to false alarms (Lenton, 2011).

Model intercomparison studies (Gregory, 2005; Stouffer et al., 2006) show no systematic differences in MOC behaviour and climate response between EMICs and GCMs (cf. Chapter 6). The multiple equilibria regime is certainly present in EMICs (De Vries and Weber, 2005; Rahmstorf et al., 2005; Weber et al., 2007) and in somewhat more complex GCMs (Hawkins et al., 2011). However, the simulations to systematically address the existence of multiple equilibrium regimes in state-of-the-art GCMs have not been performed yet.

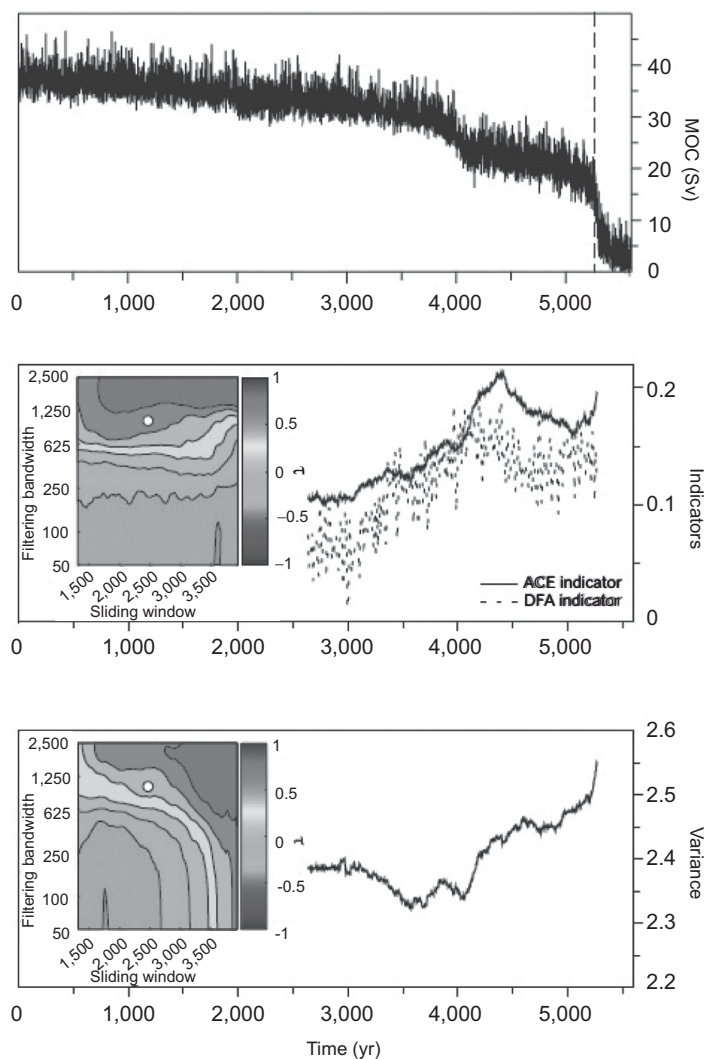


Figure 10.7 Upper panel: time series of the MOC strength as determined from an EMIC where freshwater is slowly released in the northern North Atlantic. Middle panel: Values of the ACF and DFA indicators. Bottom panel: variance of the time series. The values of τ in the inset are results from a statistical test to determine a significant increase in the value of the particular quantity (figure from Lenton, 2011). (See Colour Plate.)

10.4 Variability of the MOC: oscillations

Apart from the possibility of multiple equilibria of the MOC, the MOC is also known to have several modes of internal variability. Two essentially different types of oscillatory modes are discussed in this section: overturning (or loop) oscillations and deep-decoupling oscillations (or flushes).

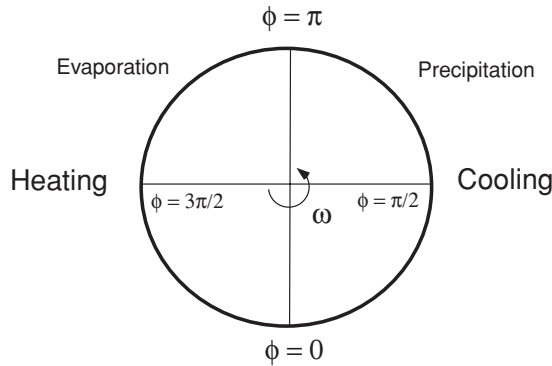


Figure 10.8 Sketch of the Howard-Malkus loop model with the anti-clockwise coordinate ϕ . The domain $\phi \in [0, \pi]$ represents the northern part of the North Atlantic. The freshwater flux is only prescribed over the domain $\phi \in [\pi/2, 3\pi/2]$.

10.4.1 Overturning oscillations

As we have seen in Chapter 9, for thermally driven flows in a single-hemispheric basin, oscillatory normal modes appear in the linear stability analysis of the North Atlantic MOC. One of these has a clear three-dimensional pattern, a multidecadal time scale and was suggested to be associated with the Atlantic Multidecadal Oscillation. However, there is another class that has a centennial time scale and which can be represented in two-dimensional models; it was called an overturning (or loop) oscillation because a central element is the propagation of the anomaly pattern along the overturning loop (Winton and Sarachik, 1993).

The Howard-Malkus loop model

Overturning (or loop) oscillations can already be found in relatively simple box models. The most elementary box model, which includes a loop oscillation, is the four-box model originally used by Huang et al. (1992) and analysed in more detail in Tziperman et al. (1994b). However, by far the best analysis of the mechanism of these oscillators can be done by using the so-called Howard-Malkus loop model (Malkus, 1972; Welander, 1986). This is a one-dimensional model of the overturning circulation representing the ocean in a circular loop, as shown in Fig. 10.8 (Sevellec et al. 2006). The angular coordinate is indicated by ϕ (positive in an anti-clockwise direction) and starts from the northern polar region. Hence the domains $\phi \in [0, \pi]$ and $\phi \in [\pi, 2\pi]$ represent the northern and southern part of the North Atlantic basin, respectively, and $\phi \in [\frac{\pi}{2}, \frac{3\pi}{2}]$ represents the upper ocean.

Mixed boundary conditions are specified along the loop, with cooling and net precipitation in the northern part and heating and net evaporation in the southern part of the basin. The spatial distribution of the restoring temperature $I^T(\phi)$ and the

Table 10.1. *Parameters of the Howard-Malkus loop model as used in Sevellec et al. (2006)*

Parameter	Meaning	Value	Unit
r_T	inverse thermal relaxation time scale	1	year ⁻¹
H	mean ocean depth	1,000	m
γ	buoyancy torque parameter	34.4	year ⁻¹
K_ϕ	lateral mixing coefficient	$2.2 \cdot 10^{-3}$	year ⁻¹
F_0	freshwater flux intensity	0.8	m year ⁻¹
α_T	thermal expansion coefficient	$2.2 \cdot 10^{-4}$	K ⁻¹
α_S	haline contraction coefficient	$7.7 \cdot 10^{-4}$	—
S_0	reference salinity	35	g kg ⁻¹
T_0	amplitude of restoring temperature	10	K

freshwater flux $I^S(\phi)$ are given by

$$I^T(\phi) = -I_{[\frac{\pi}{2}, \frac{3\pi}{2}]} \sin \phi, \quad (10.3a)$$

$$I^S(\phi) = -I_{[\frac{\pi}{2}, \frac{3\pi}{2}]} \sin 2\phi, \quad (10.3b)$$

where $I_{[a,b]}$ is the indicator function on an interval $[a, b]$.

Advection is represented by an angular velocity ω , and the angular momentum balance over the loop gives (Maas, 1994) that ω is proportional to the buoyancy torque integrated over the loop. With a linear equation of state, the equations of the Howard-Malkus loop model for the temperature T and salinity S of the fluid are given by

$$\frac{\partial T}{\partial t} + \omega \frac{\partial T}{\partial \phi} = r_T(T_0 I^T(\phi) - T) + K_\phi \frac{\partial^2 T}{\partial \phi^2}, \quad (10.4a)$$

$$\frac{\partial S}{\partial t} + \omega \frac{\partial S}{\partial \phi} = -\frac{F_0 S_0}{H} I^S(\phi) + K_\phi \frac{\partial^2 S}{\partial \phi^2}, \quad (10.4b)$$

$$\omega = -\gamma \int_0^{2\pi} (-\alpha_T T + \alpha_S S) \sin \phi \, d\phi. \quad (10.4c)$$

An explanation of the parameters of the model (and their standard value) is provided in Table 10.1. The main control parameter in this model is the freshwater flux strength F_0 .

In this model, oscillatory behaviour arises through a Hopf bifurcation as F_0 is increased, and an example of a limit cycle with a period of 170 years (for the parameters as in Table 10.1) is shown in Fig. 10.9. The period of the oscillation is very close to the mean overturning time ($2\pi/\bar{\omega}$), which indicates that the propagation of the anomalies

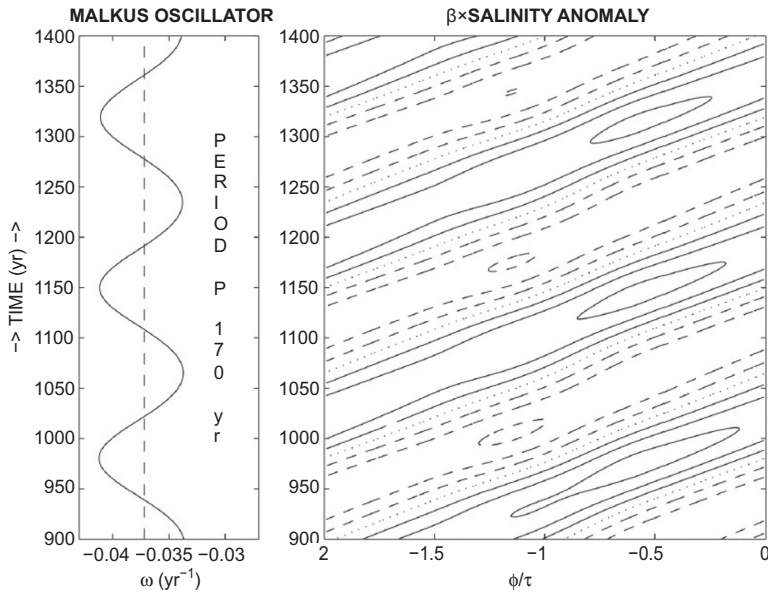


Figure 10.9 Numerical integration of the nonlinear Howard-Malkus loop model (10.4). The left panel shows the overturning ω as a function of time. In the right panel, a Hovmöller diagram of the salinity anomaly (multiplied by α_S) is plotted. The solid, dashed and dotted lines respectively correspond to positive, negative and zero anomalies; the contour interval is 0.75×10^{-4} (figure from Sevellec et al., 2006).

is governed by advection of salinity (buoyancy) anomalies by the mean overturning circulation.

The growth mechanism of the centennial oscillation was presented in detail in Sevellec et al. (2006). Consider in Fig. 10.10a a positive salinity anomaly, which is advected with the thermally driven circulation $\omega < 0$. This anomaly reduces the buoyancy torque and hence reduces the meridional overturning, represented by ω . The residence time of the anomaly in the evaporation zone is increased, which strengthens the anomaly (Fig. 10.10a). When the anomaly leaves the evaporation zone to enter the precipitation zone (Fig. 10.10b), it accelerates the meridional overturning. The residence time in the precipitation zone is hence shortened, which also amplifies the perturbation. The oscillation arises because the salinity anomaly is advected along the loop (Sevellec et al., 2006).

Ocean-only models

The overturning (or loop) oscillations as in the Howard-Malkus model are found in latitude-depth models of the double-hemispheric meridional overturning circulation (Mysak et al., 1993; Quon and Ghil, 1995; Sakai and Peltier, 1995; Dijkstra and Molemaker, 1997) and in three-dimensional models of single- and double-hemispheric ocean flows (Winton and Sarachik, 1993; Te Raa and Dijkstra, 2003a; Sevellec et al.,

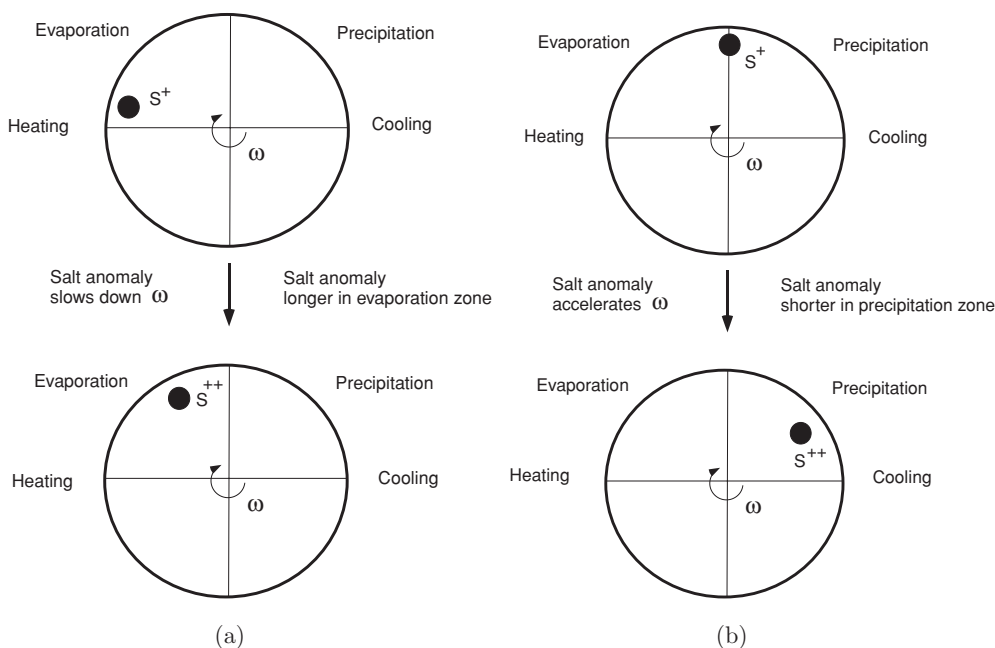


Figure 10.10 Sketch of the time evolution of salinity anomalies in the Howard-Malkus loop model leading to growth of the initial perturbation. (a) A positive salinity anomaly in the evaporation zone. (b) A positive salinity anomaly in the precipitation zone (figure redrawn from Sevellec et al., 2006).

2006). In the two-dimensional models, the oscillations arise through a Hopf bifurcation on the thermal branch, as in the Howard-Malkus model. When these oscillatory modes are damped, they can easily be excited by noise in the freshwater flux (Te Raa and Dijkstra, 2003a; Sevellec et al., 2006).

Loop oscillations are also found in multi-basin models such as those that consists of three latitude-depth ocean models, which are coupled in the south through a circum-polar channel. Sakai and Peltier (1996) find small-amplitude overturning oscillations with a centennial time scale and show that the period increases when freshwater is added to the North Atlantic. This behaviour is robust when the ocean model is coupled to an atmospheric energy balance model (Sakai and Peltier, 1997) and is consistent with their results in a single-basin model (Sakai and Peltier, 1995).

In Weijer and Dijkstra (2003), the explicit identification of multiple internal ocean modes of the global ocean circulation within a low-resolution ocean general circulation model was presented. An equilibrium state of the global ocean model was determined, and next the linear stability problem of this state was solved. It was found that all eigenvalues have negative real parts and hence that the steady solution is linearly stable. Three of the normal modes found are oscillatory and have oscillation periods of 2,000–3,000 years.

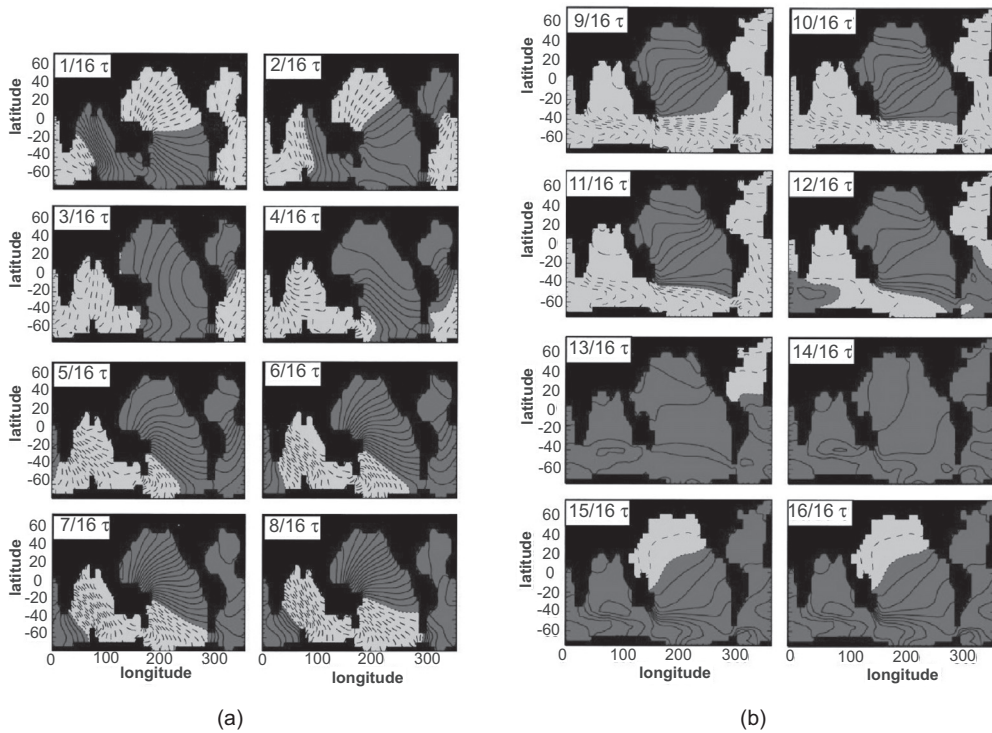


Figure 10.11 (a) Propagation of temperature anomalies at 3,000-m depth for the oscillatory mode 3 in Weijer and Dijkstra (2003) having a period τ of about 2,500 years. Positive (negative) anomalies are denoted by solid (dashed) contours and red (blue) colours. Contour levels are the same for all panels. (b) As Fig. 10.11a, but now at 500 m and showing the second half of the oscillation. (See Colour Plate.)

For the oscillatory modes in Weijer and Dijkstra (2003), the propagation of salinity anomalies displays the same pattern as that of their thermal counterparts. In fact, thermal and saline anomalies are of the same sign and largely, but not completely, density-compensating throughout the oscillations. Hence for the shortest period mode (mode 3 in Weijer and Dijkstra 2003), only the thermal anomalies are shown in Fig. 10.11.

The journey of a thermal anomaly (with oscillation period τ) can best be followed through the zero-phase line that separates negative anomalies (denoted blue) from positive anomalies (red). The anomaly (Fig. 10.11) starts off in the deep North Atlantic ($t = 2/16 \tau$), and when it reaches the Southern Ocean, it propagates eastward ($t = 6/16 \tau$) and fills the deep Indian Ocean ($t = 9/16 - 11/16 \tau$) and the Pacific Ocean ($t = 14/16 - 19/16 \tau$). However, rather than a single anomaly travelling through the deep ocean, two anomalies are present in the abyss at the same time. So when a positive anomaly sets off in the deep North Atlantic ($t = 2/16 \tau$, Fig. 10.11), another anomaly is still working its way north in the deep Pacific.

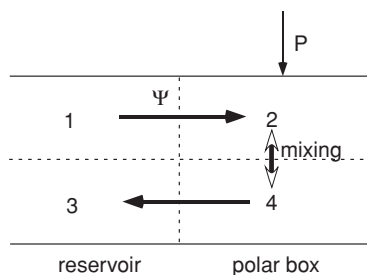


Figure 10.12 Sketch of the box model with a reservoir and a polar box with a vertical structure, here referred to as the CdV model (Colin de Verdière, 2007). The circulation Ψ is positive when the surface volume transport is northward (as indicated).

From the analysis of the propagation of temperature and salinity anomalies, it was demonstrated in Weijer and Dijkstra (2003) that these modes are the global version of the loop oscillations. Important here is that the time scale of the oscillations depend on advective transport processes, whereas the growth rate depends on diffusive processes. The internal modes in Weijer and Dijkstra (2003) are strongly damped because of the large diffusivity in their model, so noise is needed to excite them.

10.4.2 Deep-decoupling oscillations ('flushes')

Oscillatory behavior does not only occur through advective processes, but may also be induced by convective processes. This oscillatory behavior has been found in a hierarchy of ocean and climate models. The basics of the behaviour can be understood from the so-called 'flip-flop' oscillation (Welander, 1982). The origin of these, also referred to as deep-decoupling oscillations, in a single-hemisphere ocean basin is, however, best explained by a box model that combines the Welander (1982) box model with a Stommel box model of the meridional overturning (Colin de Verdière, 2007).

The box model in Fig. 10.12 consists of a reservoir (boxes 1 and 3) in which temperatures and salinities are fixed and an active polar box (boxes 2 and 4). Heat and salt are exchanged with the reservoir by advection and diffusion, and mixing occurs in the polar box when the density in box 2 becomes larger than that in box 4.

It is assumed that the surface restoring of heat is so strong that the temperature in the upper polar box T_2 is constant. Likewise, it is assumed that the salinity in the lower polar box S_4 is fixed. The meridional overturning Ψ (Ψ is taken positive when the circulation is clockwise) depends on the mean density difference between the polar box and the reservoir. With the linear equation of state,

$$\rho = \rho_0(1 - \alpha_T(T - T_0) + \alpha_S(S - S_0)),$$

where α_T and α_S are constant thermal expansion and haline contraction coefficients and T_0 and S_0 reference values, it is given by

$$\Psi = C(\alpha_T(T_1 - T_2) + \alpha_T(T_3 - T_4) - \alpha_S(S_1 - S_2) - \alpha_S(S_3 - S_4)), \quad (10.5)$$

where C is a hydraulic constant.

The equations for the temperature T_4 and S_2 follow from heat and salt balances and are given by

$$V \frac{dT_4}{dt} = \Psi^+(T_2 - T_4) + \Psi^-(T_4 - T_3) + D(T_3 - T_4), \quad (10.6a)$$

$$V \frac{dS_2}{dt} = P + \Psi^+(S_1 - S_2) + \Psi^-(S_2 - S_4) + D(S_1 - S_2), \quad (10.6b)$$

where $\Psi^+ = (\Psi + |\Psi|)/2$ and $\Psi^- = (\Psi - |\Psi|)/2$, P is the virtual salt (freshwater) flux into box 2, V is the volume of the box 2 and of box 4 (taken equal) and D is the lateral diffusion coefficient.

The dimensionless vertical density difference in the polar box $R = (\rho_2 - \rho_4)/\rho_0$ is given by

$$R = -\alpha_T(T_2 - T_4) + \alpha_S(S_2 - S_4). \quad (10.7)$$

For the stable stratification, $R < 0$ and when $R > 0$ mixing will occur. By introduction of the variables $x = -\alpha_T(T_2 - T_4)$ and $y = -\alpha_S(S_2 - S_4)$, we can write

$$\Psi = C(r_1 - (x + y)), \quad (10.8a)$$

$$R = x - y, \quad (10.8b)$$

with $r_1 = \alpha_T(T_{12} + T_{32}) - \alpha_S(S_{14} + S_{34})$, $T_{ij} = T_i - T_j$ and $S_{ij} = S_i - S_j$. The equations for x and y follow directly from (10.6) and then the equations for Ψ and R follow immediately from (10.8) as

$$V \frac{d\Psi}{dt} = F - (\Psi^+ - \Psi^- + D)\Psi + \psi_T \Psi^+ - \psi_H \Psi^-, \quad (10.9a)$$

$$V \frac{dR}{dt} = G - (\Psi^+ - \Psi^- + D)R + r_2 \Psi^+ - r_3 \Psi^-. \quad (10.9b)$$

When $R > 0$, the streamfunction is reset to the convective value. In the model this is represented by adding a term $-\mathcal{H}(R)R/\tau$ on the right-hand side of (10.9b) with a small time scale τ and \mathcal{H} being the Heaviside function. When $R > 0$, the streamfunction is then given by $\Psi = Cr_1$. In the equations, $F = C(\alpha_S P + D(\alpha_T T_{12} - \alpha_S S_{34}))$, $r_2 = \alpha_S S_{14}$, $r_3 = \alpha_T T_{32}$, $G = \alpha_S P + D(r_2 + r_3)$, $\psi_T = C(r_1 + r_2)$ and $\psi_H = C(r_1 - r_3)$. The standard values of the parameters in (10.9) are presented in Table 10.2; the main control parameter is the freshwater forcing strength P .

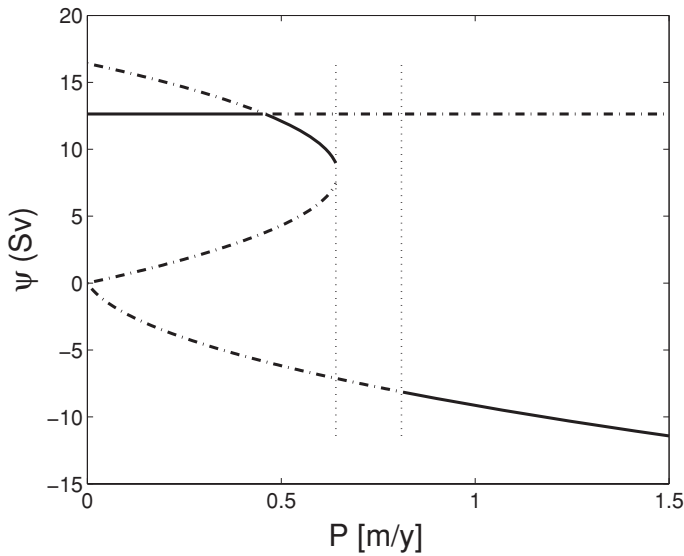
Table 10.2. *Parameters of the CdV-box model (Colin de Verdière, 2007)*

Parameter	Meaning	Value	Dimension
C	hydraulic constant	10^4	Sv
D	'lateral mixing' coefficient	4.7	Sv
V	volume of polar box	$1.24 \cdot 10^{13}$	km^3
α_T	compressibility of heat	$2 \cdot 10^{-4}$	$^{\circ}\text{C}^{-1}$
α_S	compressibility of salt	$8 \cdot 10^{-4}$	—
S_1	salinity in box 1	35.4	g kg^{-1}
T_1	temperature in box 1	9	$^{\circ}\text{C}$
T_2	temperature in box 2	3	$^{\circ}\text{C}$
T_3	temperature in box 3	8.5	$^{\circ}\text{C}$
S_3	salinity in box 3	35.2	g kg^{-1}
S_4	salinity in box 4	34.9	g kg^{-1}
τ	convective time scale	10^4	s
P	evaporation minus precipitation	0.65	m year^{-1}

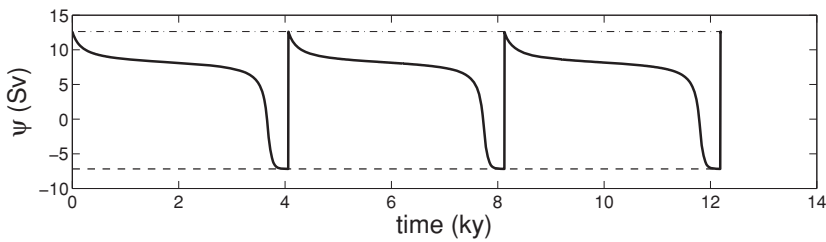
In this model, a convective branch of steady solutions (independent of P) is present in addition to the Stommel solution branch connecting the TH and SA solutions (Fig. 10.13a). In a certain interval of P , where the SA solution is unstable, millennial time-scale oscillations occur between this SA state and the unstable convective state (Fig. 10.13b). At the boundaries of this parameter interval, the period of these oscillations approaches infinity. There is first a slow decrease of the meridional overturning, during which the static stability in the polar box decreases because of a warming in the lower box. At some point, the stratification becomes unstable, which induces convection and a rapid resumption of the overturning. This type of deep-decoupling or flushing oscillatory behaviour has also been found in more extensive box models and two-dimensional models (Winton and Sarachik, 1993; Colin de Verdière et al., 2006).

10.5 Effects of noise: stochastic resonance

As can be anticipated from the material presented so far, changes in heat transport associated with transitions or oscillations in the Atlantic MOC may be a good ingredient for explaining rapid temperature changes in the northern North Atlantic associated with the D-O events. Indeed, changes in the MOC play an essential role in the two mechanisms discussed in detail next. Both mechanisms differ in their role attributed to oscillatory internal modes. The (nonautonomous) stochastic resonance theory is based only on the presence of the multiple equilibrium regime, whereas the central ingredient of the so-called coherence resonance (or autonomous stochastic resonance) mechanism is the existence of oscillatory modes with a millennial time scale.



(a)



(b)

Figure 10.13 (a) Bifurcation diagram using P as a control parameter for the standard values of the parameters. (b) Temporal evolution of Ψ for $P = 0.65$ m/yr; time is in kyr. The horizontal lines represent the values of the convective and salinity-driven steady states in (a) (figure from Colin de Verdière, 2007).

10.5.1 (Nonautonomous) stochastic resonance

We first describe the basic features of stochastic resonance using results of the stochastic Stommel two-box model. Next, the mechanism is discussed in more detail using the periodically forced stochastic pitchfork bifurcation.

Box models

From the bifurcation diagram in Fig. 10.5a, it is clear that for the range of γ_p values between L_1 and L_2 , there are two stable states. The one with a strong MOC, and with the larger northward heat transport, is usually referred to as the ‘on-state’, whereas that with the weak MOC is called the ‘off-state’. Clearly, both on-state and off-state are linearly stable, so a finite amplitude perturbation is certainly needed to induce a

transition between both states. These finite amplitude perturbations are provided by background noise, for example, in the freshwater flux.

The effect of additive noise on the transition behaviour between on and off states of the MOC was considered in a box model by Cessi (1994). This model is a variant of the Stommel two-box model presented in Example 6.1. Again, a polar box (with temperature T_p and salinity S_p) and an equatorial box (with temperature T_e and salinity S_e) having the same volume V are connected by advective flow and exchange heat and freshwater with the atmosphere. The heat and salt balances are

$$\frac{dT_e}{dt} = -\frac{1}{t_r} \left(T_e - \left(T_0 + \frac{\theta}{2} \right) \right) - \frac{1}{2} Q(\Delta\rho)(T_e - T_p), \quad (10.10a)$$

$$\frac{dT_p}{dt} = -\frac{1}{t_r} \left(T_p - \left(T_0 - \frac{\theta}{2} \right) \right) - \frac{1}{2} Q(\Delta\rho)(T_p - T_e), \quad (10.10b)$$

$$\frac{dS_e}{dt} = \frac{F_S}{2H} S_0 - \frac{1}{2} Q(\Delta\rho)(S_e - S_p), \quad (10.10c)$$

$$\frac{dS_p}{dt} = -\frac{F_S}{2H} S_0 - \frac{1}{2} Q(\Delta\rho)(S_p - S_e), \quad (10.10d)$$

where F_S is the fresh water flux, H is the ocean depth, S_0 is a reference salinity, T_0 is a reference temperature, t_r is the surface temperature restoring time scale and θ is the equator-to-pole atmospheric temperature difference. A linear equation of state of the form

$$\rho = \rho_0(1 - \alpha_T(T - T_0) + \alpha_S(S - S_0)), \quad (10.11)$$

is assumed, where the subscript '0' refers to the reference values, and α_T and α_S are constant thermal expansion and haline contraction coefficients, respectively. In Cessi (1994), the transport function Q is chosen as

$$Q(\Delta\rho) = \frac{1}{t_d} + \frac{q}{\rho_0^2 V} (\Delta\rho)^2, \quad (10.12)$$

where q is a transport coefficient, t_d a diffusion time scale and $\Delta\rho = \rho_p - \rho_e$.

Subtracting (10.10b) from (10.10a) and (10.10d) from (10.10c) and introducing $\Delta T = T_e - T_p$ and $\Delta S = S_e - S_p$ leads to

$$\frac{d\Delta T}{dt} = -\frac{1}{t_r}(\Delta T - \theta) - Q(\Delta\rho)\Delta T, \quad (10.13a)$$

$$\frac{d\Delta S}{dt} = \frac{F_S}{H} S_0 - Q(\Delta\rho)\Delta S. \quad (10.13b)$$

Table 10.3. *Parameters of the stochastic Stommel box model (slightly changed from those in Cessi [1994])*

Parameter	Meaning	Value	Unit
t_r	temperature relaxation time scale	25	days
H	mean ocean depth	4,500	m
t_d	diffusion time scale	180	years
t_a	advective time scale	29	years
q	transport coefficient	1.92×10^{12}	$\text{m}^3 \text{s}^{-1}$
V	ocean volume	$300 \times 4.5 \times 8,250$	km^3
α_T	thermal expansion coefficient	10^{-4}	K^{-1}
α_S	haline contraction coefficient	7.6×10^{-4}	—
S_0	reference salinity	35	g kg^{-1}
θ	meridional temperature difference	25	K

With the scales $\Delta T = x \theta$, $\Delta S = y \alpha_T \theta / \alpha_S$ and time scaled with t_d , the nondimensional system of equations becomes

$$\frac{dx}{dt} = -\alpha(x-1) - x(1 + \mu^2(x-y)^2), \quad (10.14a)$$

$$\frac{dy}{dt} = F - y(1 + \mu^2(x-y)^2), \quad (10.14b)$$

where $\alpha = t_d/t_r$ is the ratio of the diffusive time scale and the temperature relaxation time scale. Furthermore,

$$\mu^2 = \frac{qt_d(\alpha_T\theta)^2}{V}, \quad (10.15)$$

is the ratio of the diffusion time scale t_d and the advective time scale $t_a = V/(q(\alpha_T\theta)^2)$. Finally, the dimensionless freshwater flux parameter F is given by

$$F = \frac{\alpha_S S_0 t_d}{\alpha_T \theta H} F_S. \quad (10.16)$$

Typical values of the dimensional parameters as motivated in Cessi (1994) are shown in Table 10.3. The volume V is based on the area of transport near the western boundary, and the q is determined from the strength of the southward branch of the MOC.

From these values, we see that α is large, as indeed the diffusion time scale is much larger than the temperature-restoring time scale. For large α , one can approximate $x = 1 + \mathcal{O}(1/\alpha)$, and the equation (10.14b) then becomes

$$\frac{dy}{dt} = F - y(1 + \mu^2(1-y)^2). \quad (10.17)$$

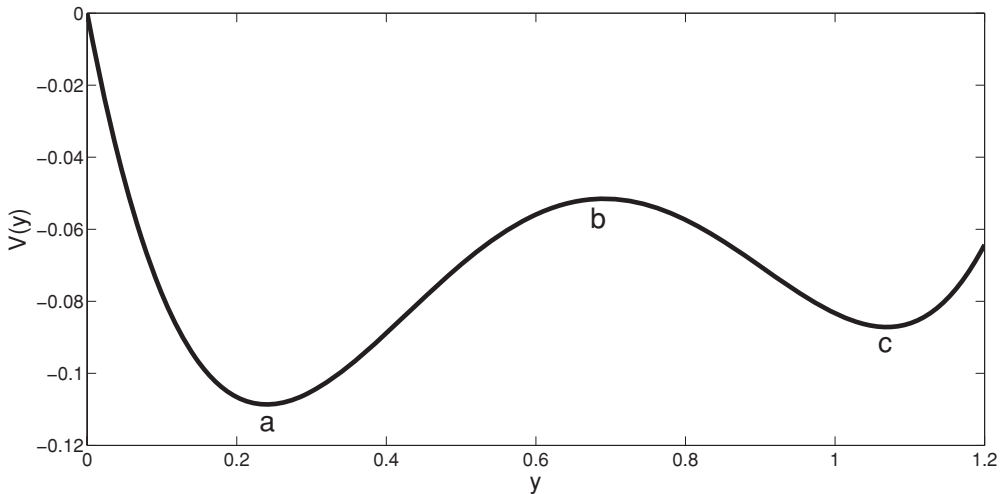


Figure 10.14 Potential $V(y)$ as in (10.19) for $\bar{F} = 1.1$ and $\mu^2 = 6.2$.

When the freshwater flux is time independent, say $F = \bar{F}$, this equation can be written as

$$\frac{dy}{dt} = -V'(y), \quad (10.18)$$

with the potential function

$$V(y) = -\bar{F}y + \frac{y^2}{2} + \mu^2 \left(\frac{y^4}{4} - \frac{2y^3}{3} + \frac{y^2}{2} \right), \quad (10.19)$$

with the prime in (10.18) indicating differentiation to y .

For $\bar{F} = 1.1$ and $\mu^2 = 6.2$, this potential is plotted in Fig. 10.14. It is a typical so-called double-well potential with minima at $y_a = 0.24$ and $y_c = 1.07$ and a maximum at $y_b = 0.69$. As extrema of $V(y)$ are the steady states of (10.18), we see immediately that the dynamical system (10.17) has three steady states. The linear stability of these steady states is directly related to the sign of the second derivative of the potential at the extrema, and hence y_a and y_c are linearly stable steady states, and y_b is an unstable steady state.

Consider now that the freshwater flux has a stochastic component, say $F = \bar{F} + \tilde{F}$, with \tilde{F} being additive white noise (i.e., represented by a Wiener process) with amplitude σ ; then (10.18) generalises into the Itô equation,

$$dY_t = -V'(Y_t)dt + \sigma dW_t. \quad (10.20)$$

A trajectory of (10.20) for $\bar{F} = 1.1$, $\mu^2 = 6.2$ and $\sigma = 0.2$ is plotted in Fig. 10.15a. As can be seen, the trajectory undergoes transitions between the two stable states (y_c and y_a). When a histogram is made of the y position, the probability density function in Fig. 10.15b results (dashed curve), which indeed shows a bimodal distribution.

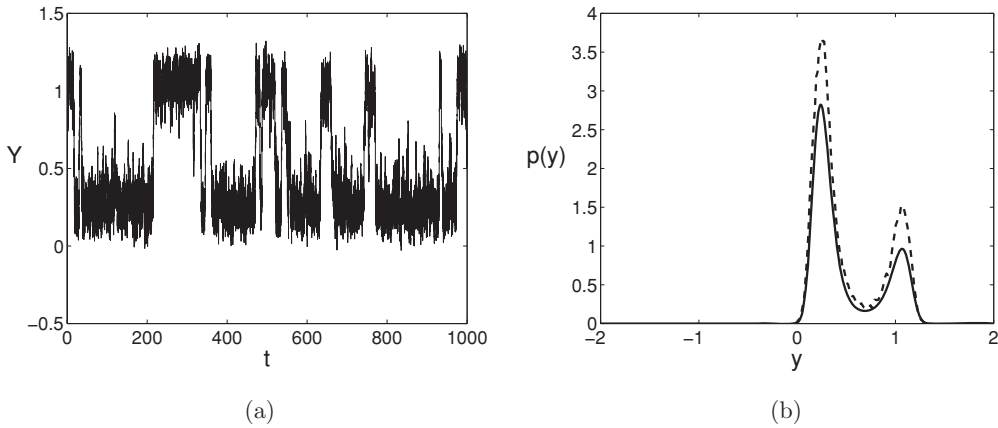


Figure 10.15 (a) Realisation of the system (10.20) using $dt = 0.01$ in a Euler-Maruyama scheme (see Section 3.6) for $\bar{F} = 1.1$, $\mu^2 = 6.2$ and $\sigma = 0.2$. (b) Non-normalised probability density function (dashed) of the simulation in (a) using 100 bins to sample the histogram. The drawn curve is the normalised analytical solution of the steady probability density function (10.22).

The probability density function $p(y, t)$ is determined from the forward Fokker-Planck equation of (10.20), see Section 3.5, which is

$$\frac{\partial p}{\partial t} - \frac{\partial(V'(y)p)}{\partial y} - \frac{\sigma^2}{2} \frac{\partial^2 p}{\partial y^2} = 0. \quad (10.21)$$

The stationary solution $p(y)$ can be easily solved as

$$p(y) = C e^{-\frac{2V(y)}{\sigma^2}}, \quad (10.22)$$

where C is a normalisation constant such that $\int p(y) dy = 1$. This stationary probability density function is also plotted in Fig. 10.15b as the drawn curve.

In Section 3.5.3, we showed that it was possible to determine how long it takes to leave the neighbourhood of one of the potential wells from a certain initial condition. Because this time is controlled by the time to go over the potential barrier at y_b , the precise specification of the initial condition and the final position is not needed. All points to the left of y_b , for example, can be considered as an ensemble, and one can define a mean escape time $\langle t_{a \rightarrow c} \rangle$ from the potential well with a minimum at y_a to the one with the minimum at y_c and vice versa ($\langle t_{c \rightarrow a} \rangle$). Expressions of these type of transition times were provided in Section 3.5.4 (Example 3.4) and for the problem (10.20) become (Cessi, 1994)

$$\langle t_{a \rightarrow c} \rangle \approx \frac{2}{\sigma^2} \int_{y_a}^{y_c} e^{\frac{2V(y)}{\sigma^2}} dy \int_{-\infty}^{y_b} e^{-\frac{2V(z)}{\sigma^2}} dz, \quad (10.23a)$$

$$\langle t_{c \rightarrow a} \rangle \approx \frac{2}{\sigma^2} \int_{y_a}^{y_c} e^{\frac{2V(y)}{\sigma^2}} dy \int_{y_b}^{\infty} e^{-\frac{2V(z)}{\sigma^2}} dz. \quad (10.23b)$$

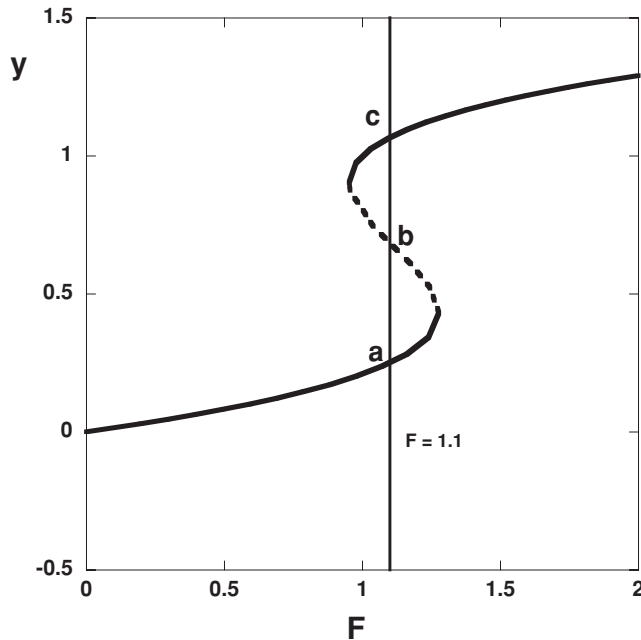


Figure 10.16 Bifurcation diagram of the model (10.14) for $\alpha = 360$ and $\mu^2 = 6.25$, with \bar{F} as control parameter (figure based on Velez-Belchi et al., 2001).

We now turn now to the full system (10.14) and take $\alpha = 360$ and $\mu^2 = 6.25$ (Velez-Belchi et al., 2001). The bifurcation diagram of this model is plotted in Fig. 10.16, where the steady-state value of y is plotted versus \bar{F} . This is qualitatively the same diagram as that of the original Stommel model, akin to Fig. 10.4a, with two stable states: the on-state (small salinity difference y) and the off-state (large salinity difference y).

With noise added to the freshwater flux, the transitions between the on- and off-states (cf. Fig. 10.15a) are not very regular and cannot serve as a prototype to explain a specific period such as that appears in the D-O events. The box model (10.14) was therefore extended to include a periodic forcing (Velez-Belchi et al., 2001) by choosing (\bar{F} again indicates the noise component)

$$F(t) = \bar{F} + A \sin\left(2\pi \frac{t}{T}\right) + \tilde{F}, \quad (10.24)$$

with $\bar{F} = 1.1$. The periodic forcing has an amplitude A in the freshwater flux and a dimensionless period T (the dimensional value can be obtained by multiplying with the diffusion time scale t_d).

The time series of the dimensionless transport q from this model for $T \times t_d = 42$ kyr (corresponding to variations associated with the obliquity cycle) and $A = 0.05$ are shown in Fig. 10.17a. Here the stochastic component \tilde{F} is zero mean Gaussian

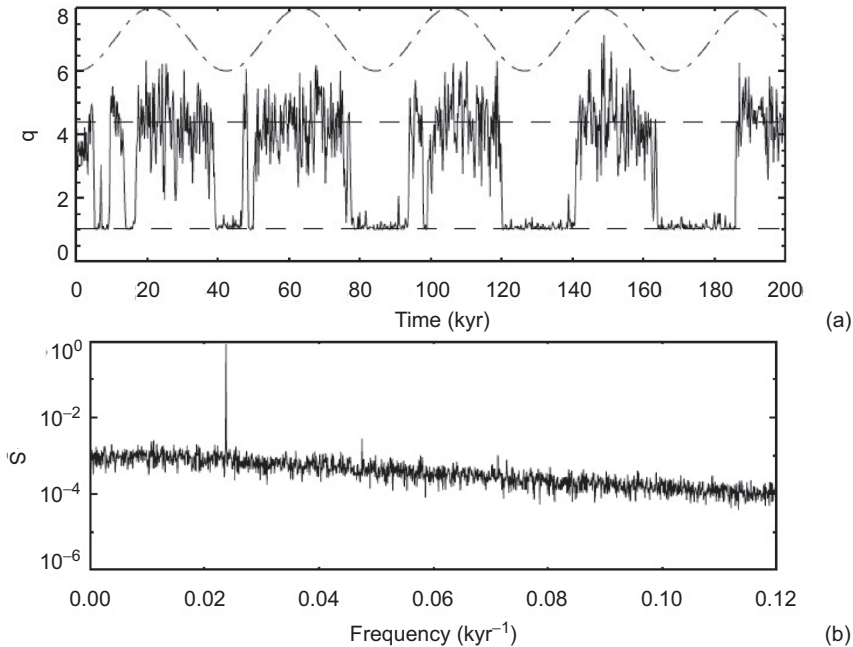


Figure 10.17 (a) Time series (drawn curve) of the transport q between the basins for the periodically and stochastically forced model (10.14), for $T \times t_d = 42$ kyr, $A = 0.05$ and $\epsilon = 0.022$. (b) Power spectrum of the trajectory in (a) (figure from Velez-Belchi et al., 2001).

noise with variance ϵ . The results show that the transitions between the stable states are clearly influenced by the periodic forcing and now become more regular. The spectrum in Fig. 10.17b indicates a red noise background with a sharp spectral peak at the forcing frequency. Apparently the very small periodic signal is amplified by the noise in the nonlinear system having a multiple equilibrium regime; such an amplification is called stochastic resonance.

A characteristic of stochastic resonance is the signal to noise ratio Σ , as measured by

$$\Sigma = 10 \log_{10} \frac{S(\omega_0)}{B}, \quad (10.25)$$

where $\omega_0 = 2\pi/T$ is the forcing frequency, $S(\omega_0)$ the power associated with that frequency and B the background spectrum of the noise. The value of Σ first increases with the noise variance, reaching a maximum value corresponding to the maximum cooperation between the periodic forcing and the noise. For large values of the noise, the transitions will be noise dominated, which is shown as a decay in Σ . In the computations in Velez-Belchi et al. (2001) with the model (10.14), the result for Σ is plotted in Fig. 10.18 for different values of the forcing period showing this characteristic

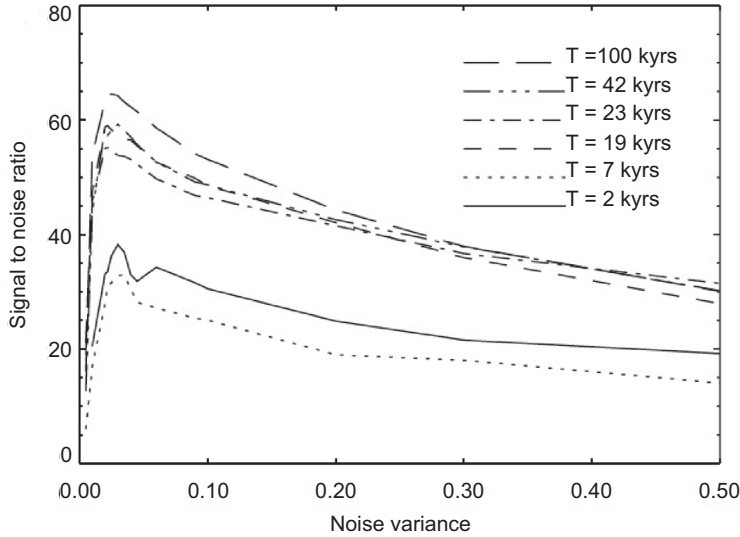


Figure 10.18 Curves of the signal to noise ratio Σ for the periodically and stochastically forced model (10.14) versus the noise variance ϵ as computed in Velez-Belchi et al. (2001).

signature of stochastic resonance. The amplification of the signal happens at small noise amplitude and for a large range of forcing frequencies.

Mechanism of stochastic resonance

To understand the stochastic resonance mechanism in more detail, we consider a sinusoidal temporal deterministic forcing in the problem of the pitchfork bifurcation with additive stochastic noise (cf. Section 4.3). The problem becomes the Itô SDE

$$X_t = X_0 + \int_0^t (X_s - X_s^3 + A \cos \Omega \tau) ds + \int_0^t \sigma dW_s, \quad (10.26)$$

where τ is considered as a parameter. The potential $V(x)$ associated with (10.26) is

$$V(x) = -\frac{1}{2}x^2 + \frac{1}{4}x^4 - Ax \cos \Omega \tau. \quad (10.27)$$

For $A = 0.1$, this potential is plotted for three values $\tau = 0$, $\tau = \pi/(2\Omega)$ and $\tau = \pi/\Omega$ in Fig. 10.19. Although the fixed point locations do not depend strongly on τ , the actual values of $V(x)$ at these fixed points do.

Central to stochastic resonance is the relative magnitude of the mean transition times with respect to the periodic forcing. The transition times are given by (10.23),

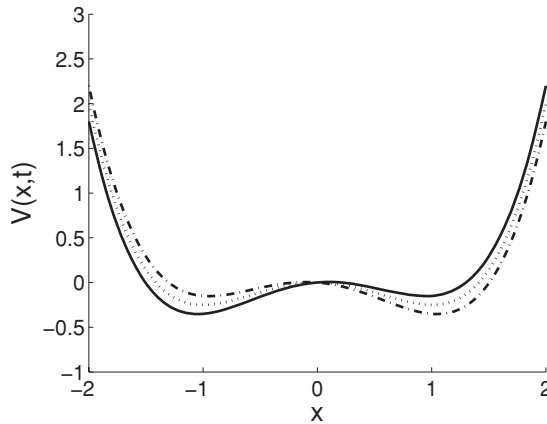


Figure 10.19 The potential $V(x)$ for three values of $\tau = 0$ (dash-dotted), $\tau = \pi/(2\Omega)$ (dotted) and $\tau = \pi/\Omega$ (solid).

with $y_a = -1$, $y_b = 0$ and $y_c = 1$, and become

$$\langle t_{-1 \rightarrow 1} \rangle \approx \frac{2}{\sigma^2} \int_{-\infty}^0 e^{-\frac{2V(x)}{\sigma^2}} dx \int_{-1}^1 e^{\frac{2V(x)}{\sigma^2}} dx, \quad (10.28a)$$

$$\langle t_{1 \rightarrow -1} \rangle \approx \frac{2}{\sigma^2} \int_0^{\infty} e^{-\frac{2V(x)}{\sigma^2}} dx \int_{-1}^1 e^{\frac{2V(x)}{\sigma^2}} dx. \quad (10.28b)$$

Here it is assumed that the equilibration time scale of the probability density function is much faster than the change in the potential. Because σ^2 is a small parameter, the integrals in (10.28) can be approximated using a method due to Laplace.

The integrals are of all of the form

$$\int_a^b e^{Mf(x)} dx, \quad M \rightarrow \infty. \quad (10.29)$$

When $f(x)$ has a positive maximum $x_0 \in (a, b)$, then the largest contribution of the integral will come from function values near x_0 . When $f(x)$ is expanded in a Taylor series near x_0 , we find (note that $f'(x_0) = 0$ and $f''(x_0) < 0$)

$$f(x) = f(x_0) - \frac{1}{2}|f''(x_0)|(x - x_0)^2 + \dots,$$

and the integral (10.28) can be approximated by

$$\begin{aligned} \int_a^b e^{Mf(x)} dx &\approx e^{Mf(x_0)} \int_a^b e^{-\frac{M}{2}|f''(x_0)|(x-x_0)^2} dx, \\ &\approx e^{Mf(x_0)} \int_{-\infty}^{\infty} e^{-\frac{M}{2}|f''(x_0)|(x-x_0)^2} dx, \end{aligned} \quad (10.30)$$

because the integrand decays very rapidly from x_0 . Using

$$\int_{-\infty}^{\infty} e^{-\alpha(x-x_0)^2} dx = \sqrt{\frac{\pi}{\alpha}},$$

it is eventually found (with $\alpha = \frac{M}{2}|f''(x_0)|$) that

$$\int_a^b e^{Mf(x)} dx \approx \sqrt{\frac{2\pi}{M|f''(x_0)|}} e^{Mf(x_0)}. \quad (10.31)$$

Using the Laplace approximation in the integrals in (10.28), we find that (with $f(x) = -V(x)$, $M = 2/\sigma^2$ and $p(x)$ as in (10.22))

$$\int_{-\infty}^0 p(x) dx = C \sqrt{\frac{\pi\sigma^2}{V''(-1)}} e^{-\frac{2V(-1)}{\sigma^2}}, \quad (10.32a)$$

$$\int_{-1}^1 \frac{1}{p(x)} dx = C^{-1} \sqrt{\frac{\pi\sigma^2}{-V''(0)}} e^{\frac{2V(0)}{\sigma^2}}, \quad (10.32b)$$

and, finally,

$$\langle t_{-1 \rightarrow 1} \rangle \approx 2\pi \sqrt{\frac{1}{-V''(0)V''(-1)}} e^{\frac{2(V(0)-V(-1))}{\sigma^2}}, \quad (10.33a)$$

$$\langle t_{1 \rightarrow -1} \rangle \approx 2\pi \sqrt{\frac{1}{-V''(0)V''(1)}} e^{\frac{2(V(0)-V(1))}{\sigma^2}}. \quad (10.33b)$$

The transition times for the potential (10.27), with $V(0) = 0$, $V(-1) = -1/4 + A \cos \Omega\tau$, $V(1) = -1/4 - A \cos \Omega\tau$, $V''(\pm 1) = 2$ and $V''(0) = -1$, are finally given by

$$\langle t_{-1 \rightarrow 1} \rangle \approx \frac{\pi}{\sqrt{2}} e^{\frac{1}{2\sigma^2}(1-4A \cos \Omega\tau)}, \quad (10.34a)$$

$$\langle t_{1 \rightarrow -1} \rangle \approx \frac{\pi}{\sqrt{2}} e^{\frac{1}{2\sigma^2}(1+4A \cos \Omega\tau)}. \quad (10.34b)$$

The important element is that the transition times vary with τ as the depth of the potential wells deepens and shallows. Suppose now that, at $\tau = 0$, the state of the system is near $x = 1$. At that time, the transition time $\langle t_{1 \rightarrow -1} \rangle$ is maximal (as the potential well is deepest), but it decreases with time until it becomes a minimum at $\tau = \pi/\Omega$. Consequently, over the time interval $[0, \pi/\Omega]$ the probability to exit the potential well near $x = 1$ increases. When the transition time $\langle t_{1 \rightarrow -1} \rangle$ at $\tau = 0$ is on the order of the time scale of the periodic forcing and the transition time at $\tau = \pi/\Omega$ is much smaller than the time scale of the periodic forcing, then the system will surely exit the well near $x = 1$ at $\tau \sim \pi/\Omega$. Once in the other well, the same reasoning can be applied using the transition time $\langle t_{-1 \rightarrow 1} \rangle$.

Because the variance in the transition time is much smaller than the transition time itself, the transition occurs over a small, well-defined time interval. Consequently, the Fourier spectra of the sample paths have a strong peak at the forcing frequency Ω . Hence the noise amplifies the periodic signal by establishing a coherent transition from one well to the other. Stochastic resonance provides a mechanism by which a small-amplitude periodic signal and noise work together to induce well-defined transitions between different states. Neither noise nor the weak periodic forcing can do this by itself.

10.5.2 Coherence resonance

Again, we discuss the basic features using the results of a box climate model and then describe the mechanism in more detail using a two-dimensional random dynamical system.

A climate box model

Using an ocean box model coupled to a simple (box type) representation of the atmosphere and sea ice, the mechanisms of millennial climate variability were analysed in Timmermann et al. (2003b). This model is discussed in more detail in Section 11.4 as it was originally used (Gildor and Tziperman, 2000) for studying the Pleistocene ice ages.

The response of the model to freshwater input in the most northern ocean box was studied. In the left panel of Fig. 10.20, the hysteresis diagram of the MOC is shown for the deterministic case (no noise in the freshwater flux) for two different rates of quasi-equilibrium change (0.001 Sv/1,000 years and 0.01 Sv/1,000 years). The very slow variation (0.001 Sv/1,000 years) results in behaviour expected from the Stommel-type bifurcation diagram with transitions between the on-state and the off-state of the MOC. Using a faster change (0.01 Sv/1,000 years) results in a transition to a large-amplitude MOC state. Under noise in the freshwater forcing, one also observes oscillatory behaviour near the transition from the on- to the off-state with an amplitude of about 4 Sv in the MOC (right panel of Fig. 10.20).

The character of these oscillations was studied by releasing a meltwater pulse of a specific amplitude for 300 years in the northern ocean box (Fig. 10.21). Under a large-amplitude (0.45 Sv) meltwater input and in the presence of noise, oscillations appear in the MOC. These oscillations have a regular, relaxation type behaviour with a rapid warming of the atmosphere and a slow cooling. Timmermann et al. (2003b) showed that the time scale of the oscillations is strongly dependent on the vertical diffusivity in their model and indicate that the mechanism can be described by a deep-decoupling oscillation.

A very interesting result is found when the response to different amplitudes of the freshwater noise is considered (again for the 0.45 Sv meltwater pulse). When

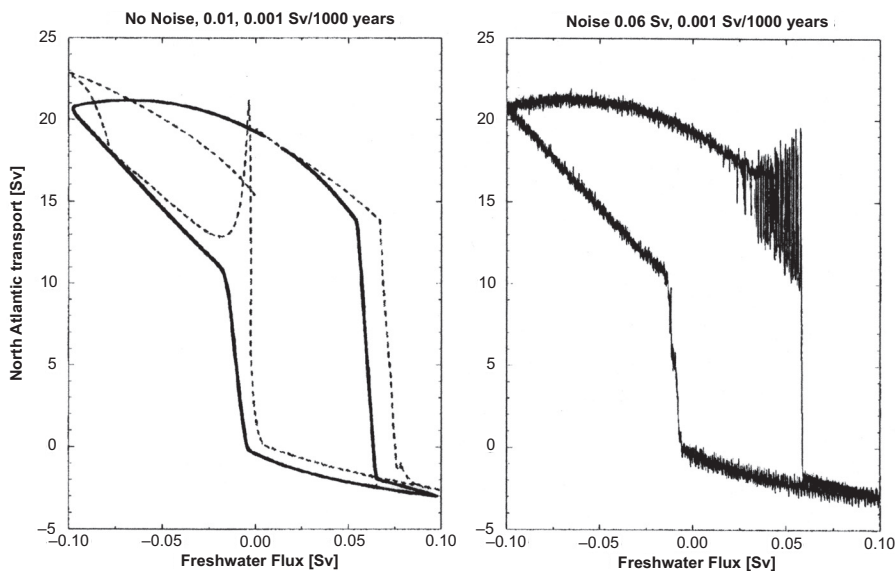


Figure 10.20 Solid lines show North Atlantic MOC transport as a function of slowly modified freshwater flux (left) without stochastic forcing and (right) with a stochastic freshwater component with an amplitude of 0.06 Sv. Transient simulations are performed in which the freshwater flux is changed linearly at a rate of 0.001 Sv per 1,000 years. Dashed line at left shows transient simulations performed in which the freshwater flux is changed linearly at a rate of 0.01 Sv per 1,000 years (figure from Timmermann et al., 2003b).

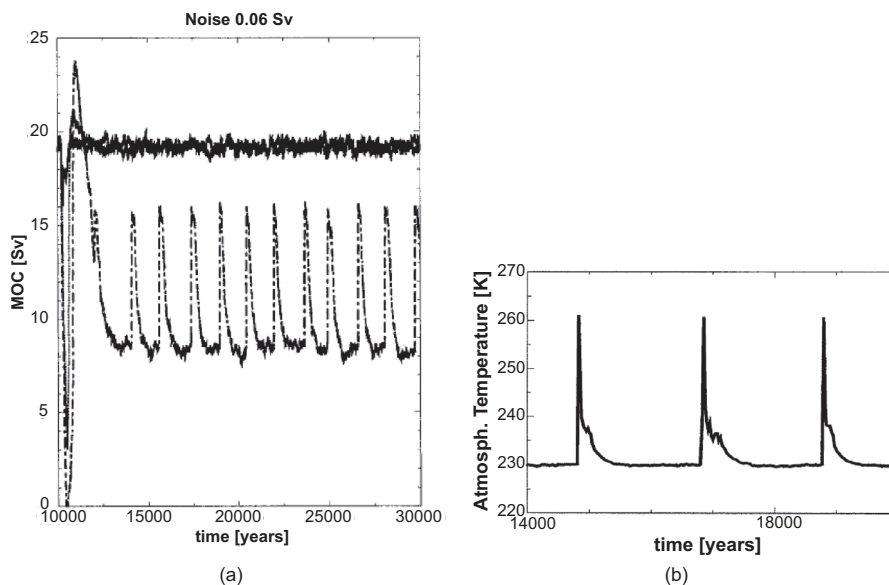


Figure 10.21 (a) Response of the North Atlantic MOC (in Sv) to a 300-year-long meltwater pulse of varying amplitude in the presence of a 0.06-Sv amplitude noise forcing in the freshwater flux. (b) January atmospheric surface temperature in the northernmost box during the oscillation in (a) for a meltwater pulse of 0.45 Sv (figure from Timmermann et al., 2003b).

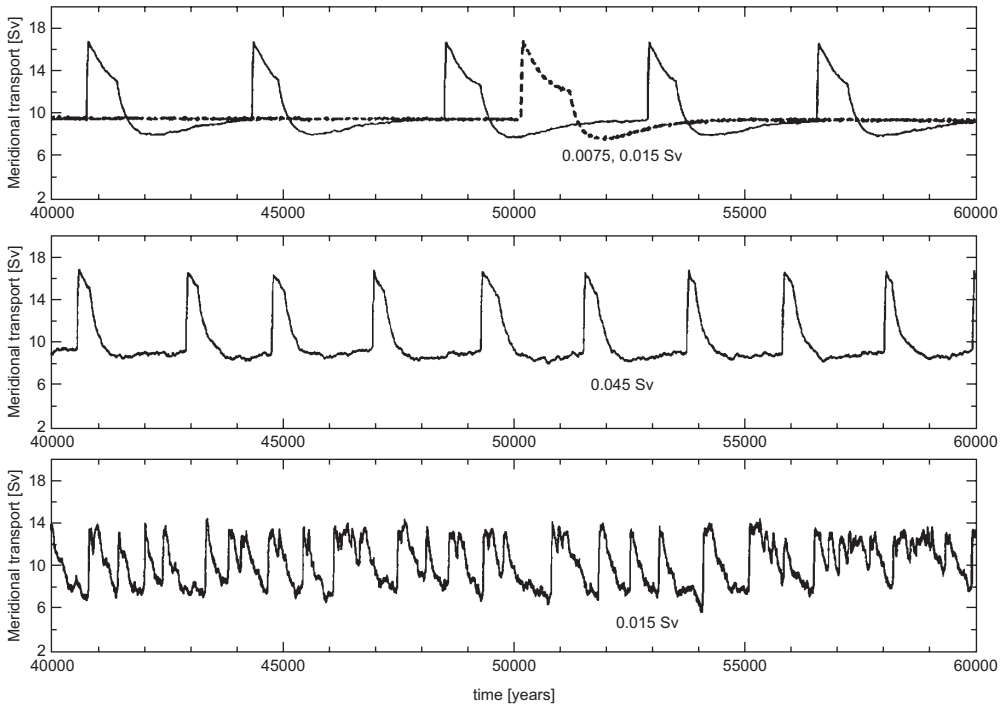


Figure 10.22 Response of the North Atlantic MOC to different stochastic freshwater forcing amplitudes (for a meltwater pulse of 0.45 Sv) (figure from Timmermann et al., 2003b).

noise is absent, there are no millennial oscillations, but they appear under a small noise amplitude (Fig. 10.22, upper panel). When the noise amplitude is very large, the millennial oscillations disappear (Fig. 10.22, lower panel), or at least the period becomes much shorter. From the middle panel in Fig. 10.22, it is seen that there seems to be an optimal noise amplitude to give the most regular millennial oscillations. These characteristics are typical for a phenomenon called coherence resonance, which is discussed in more detail next. Note that no periodic forcing is needed in coherence resonance, in contrast to the classical (nonautonomous) stochastic resonance.

Basic mechanism of coherence resonance

The phenomenon of coherence resonance was first found in the noise-driven fast-slow systems (Section 3.5.5.), in particular in the so-called FitzHugh-Nagumo model (Pikovsky and Kurths, 1997). The equations of this model are the two-dimensional Itô system (for $a > 0$),

$$\epsilon dX_t = \left(X_t - \frac{1}{3} X_t^3 - Y_t \right) dt, \quad (10.35a)$$

$$dY_t = (X_t + a)dt + D dW_t. \quad (10.35b)$$

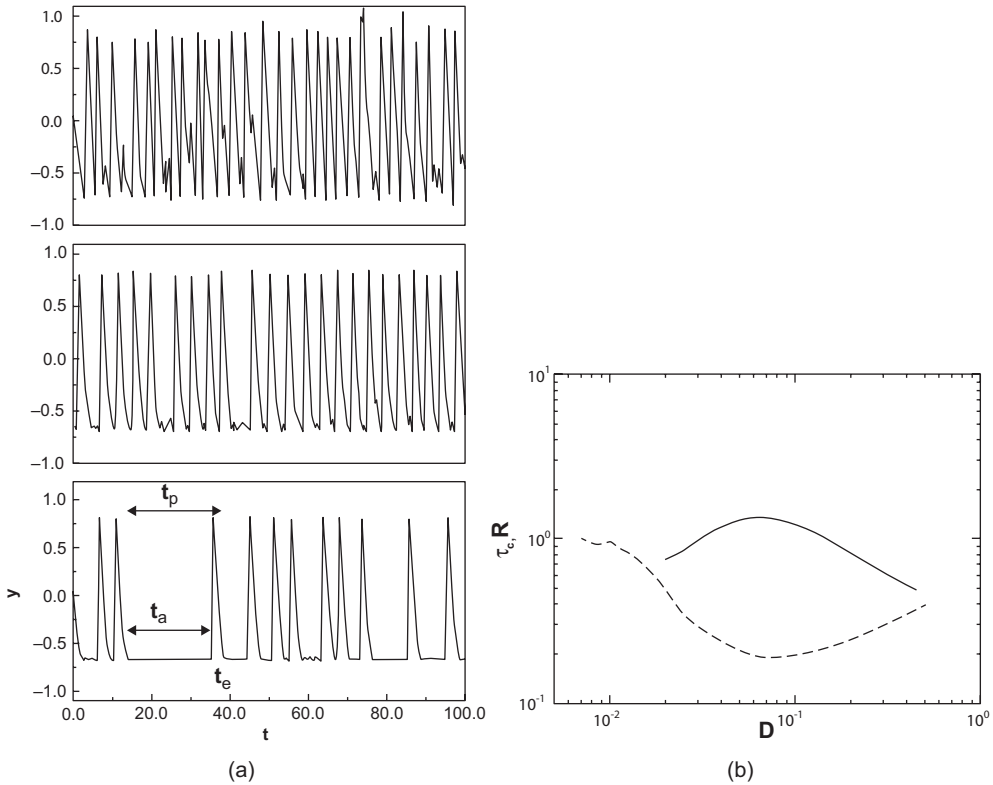


Figure 10.23 (a) Trajectories of Y_t for $a = 1.05$, $\epsilon = 0.01$ and different noise amplitudes D , from top to bottom given by $D = 0.02$, $D = 0.07$ and $D = 0.25$. (b) Characteristic correlation time τ_c (solid) and normalised fluctuations of pulse durations R (dashed) of the signal in (a) (figure from Pikovsky and Kurths, 1997).

The deterministic system has a fixed point $x = -a$, $y = a - a^3/3$, and the linear stability of the fixed point indicates that it is stable for $a > 1$ and unstable for $a < 1$. The eigenvalues of the Jacobian matrix are a complex conjugate pair near $a = 1$, and hence a Hopf bifurcation occurs at $a = 1$.

For a slightly larger than 1, the system is excitable by the noise, as the limit cycle is ‘nearby’. For $a = 1.05$ and $\epsilon = 0.01$, the behaviour of Y_t is shown for different noise amplitudes D in Fig. 10.23a. To investigate the degree of coherence in the time series, the characteristic correlation time τ_c and the normalised fluctuations of pulse durations R defined by

$$\tau_c = \int_0^\infty C^2(\tau) d\tau ; C(\tau) = \frac{\langle \tilde{Y}_t \tilde{Y}_{t+\tau} \rangle}{\langle \tilde{Y}_t^2 \rangle}, \quad (10.36a)$$

$$R = \frac{\sqrt{\text{Var}(t_p)}}{\langle t_p \rangle}, \quad (10.36b)$$

are computed, where $\tilde{Y}_t = Y_t - \langle Y_t \rangle$ is the anomaly with respect to mean (indicated by the brackets). There seems to be an optimal noise amplitude for τ_c to be a maximum and R to be minimum (Fig. 10.23b).

The appearance of this coherence resonance is tightly coupled to the excitable nature of this system: the development of the system has two characteristic time scales. An activation time scale t_a is needed to excite the system from the stable fixed point, whereas the excursion time t_e is the time needed to return from the excited state to the fixed point. Both times are indicated in Fig. 10.23a (bottom panel). The pulse duration is the sum of these times, $t_p = t_a + t_e$. For small noise, it takes very long to excite the system, and hence $t_a \gg t_e$ and the pulse time is controlled by the activation time. For large noise amplitude, the activation time is very small, and hence the pulse time is dominated by the excursion time t_e . The coherence resonance appears under a noise level where the threshold of excitation is small (such that $t_a \ll t_e$) but not very large so that fluctuations in the excursion time are small.

10.6 Climate models

The box models of which the results were discussed in the previous sections have relatively few degrees of freedom. These models can represent the multiple equilibrium regime and basic oscillation mechanisms of the Atlantic MOC but, for example, not the effect of different external climate conditions such as the difference in MOC stability under present-day and glacial climate conditions (relevant for the D-O events).

The effect of background climate conditions on MOC stability was explored in Ganopolsky and Rahmstorf (2001) using an EMIC (Climber-2), cf. Chapter 6. By varying the freshwater forcing in two different regions, the hysteresis signature was explored in this model for both the present-day climate and the climate of the Last Glacial Maximum (LGM). The hysteresis is broad for the present-day situation (Fig. 10.24a,c), for which there is a transition between the on- and off-states (Fig. 10.25a,c). However, the hysteresis is nearly absent for the LGM (Fig. 10.24b,d). The off-state does not seem to exist, and the only stable circulation is the weak MOC pattern, in Fig. 10.25d referred to as the ‘cold’ state. However, for slightly negative freshwater forcing, the system can jump to an LGM ‘warm’ state (Fig. 10.25b), but this state does not appear to be an equilibrium state of the model.

For the LGM climate, a periodic forcing in the North Atlantic (over the domain 50–80°N) with an amplitude of 0.03 Sv was applied. When the freshwater flux is slightly negative, a transition from the cold to the warm state is induced (the transition B in Fig. 10.24), which leads to a rapid warming of the North Atlantic climate (Fig. 10.26). Because the warm state is not stable, it decays due to the input of freshwater, which weakens the MOC. This gives the slow cooling phase, which lasts until the freshwater anomaly is negative again, leading to a new transition to the warm state. The MOC changes over this cold-warm transition are enormously large (about 30 Sv), as are the

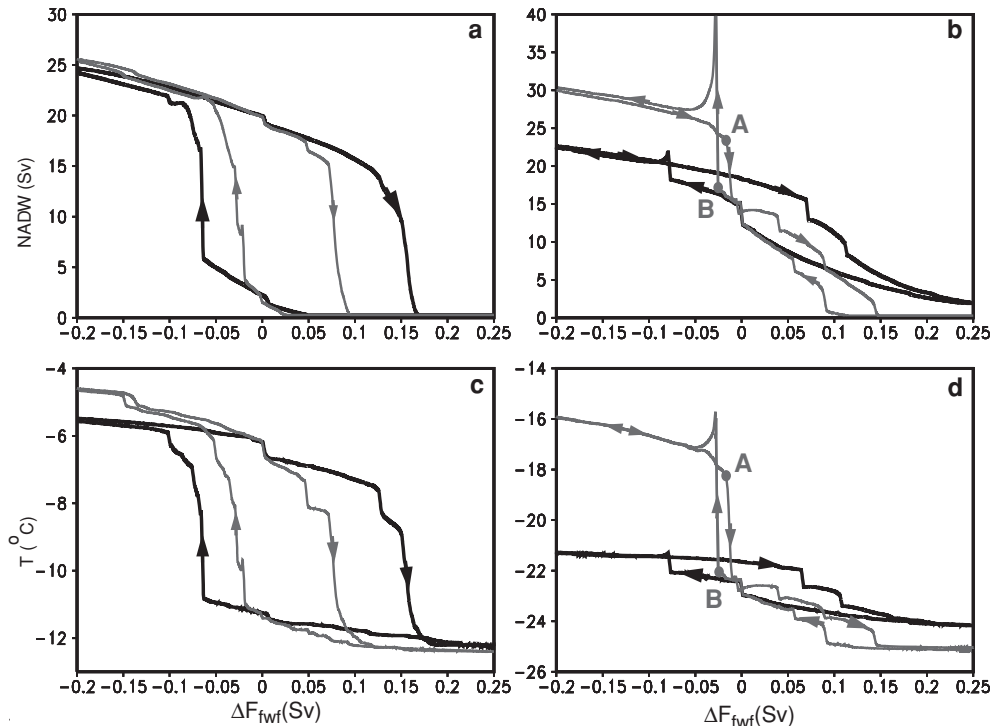


Figure 10.24 Results of quasi-equilibrium computations with the Climber-2 (EMIC) model where a freshwater anomaly is applied in two different regions (dark: 20–50°N, light: 50–70°N). The curves in (a) and (c) are for the present-day climate, whereas curves (b) and (d) are for the LGM (figure from Ganopolsky and Rahmstorf, 2001).

changes in surface heat flux, which provides the strong changes in surface temperature over the North Atlantic sector (Fig. 10.26d). The temperature changes over Antarctica (Fig. 10.26e) are smaller and for the large freshwater amplitude event labelled 3 out of phase with those in the North Atlantic.

The combined effect of noise and a weak periodic forcing (0.01 Sv) was studied within the same model (Ganopolski and Rahmstorf, 2002). When only noise in the freshwater forcing is considered (with a standard deviation of 0.035 Sv), the transitions are irregularly spaced. However, when the weak periodic forcing is included, the combined effect with the noise leads to a synchronisation of the events (Fig. 10.27). Although the periodic forcing here is too weak to cause transitions from the cold state to the warm state, the noise is able to induce these transitions and to synchronise them according to the stochastic resonance mechanism. This type of stochastic resonance is not the same as that in double-well potential discussed in Section 10.5.1, as here there are no two stable equilibrium states.

In Ganopolski and Rahmstorf (2002), the rate of change of the freshwater flux is relatively large. Hence the excitable warm state they find is likely due to a transition

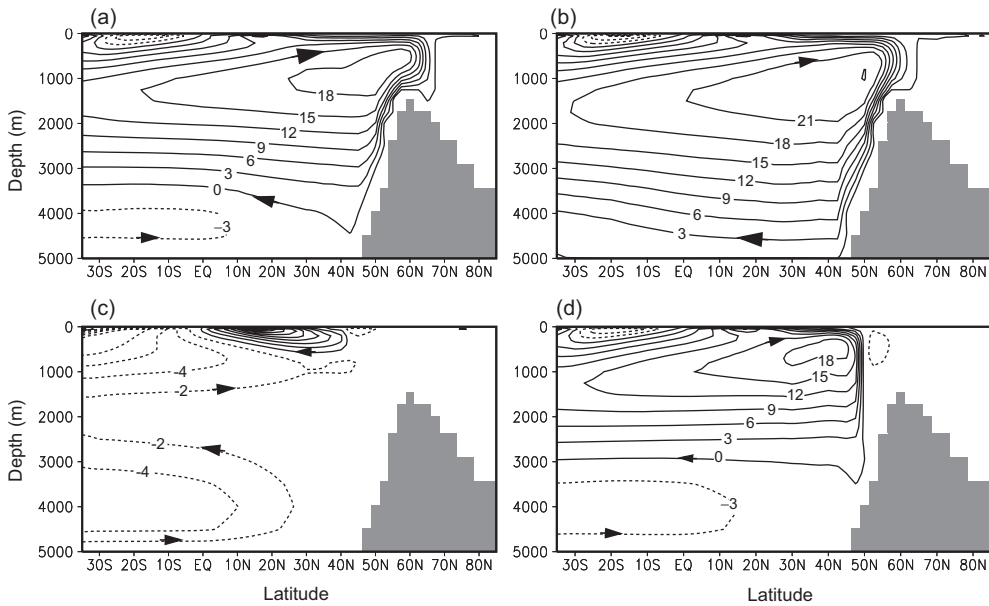


Figure 10.25 Patterns of the equilibrium Atlantic MOC (contours in Sv) in the Climber-2 model. (a) On- and (c) off-state of the Atlantic MOC in the present-day climate. (b) MOC of the excited warm state of the LGM climate and (d) MOC of the cold state of the LGM (figure from Ganopolsky and Rahmstorf, 2001).

to a transient excursion to an orbit associated with the deep-decoupling oscillation. The amplitude of the signal and its spatial pattern seems indeed to correspond to this type of oscillation. In this case, the effect of noise is to synchronise the transitions between the cold and the excited warm state, which is not the traditional stochastic resonance case but dynamics referred to as ‘ghost’ resonance (Braun et al., 2007). So in this model there likely is oscillatory variability associated with deep-decoupling oscillations. The periodic forcing is needed to cause this ‘ghost’ transition, and a possible origin of this forcing was suggested to be solar variability (Braun et al., 2005).

10.7 Synthesis

Here we summarise and discuss what dynamical systems theory has taught us about the dynamics of the D-O events, in particular about the time scale and spatial pattern. We restricted the discussion to mechanisms in which the Atlantic MOC was involved; mechanisms for this variability that do not involve changes in the MOC have been suggested as well (for an overview, see Clement and Peterson, 2008), but have major problems in explaining the dominant time scale and spatial pattern of the variability, and hence we have not discussed them here.

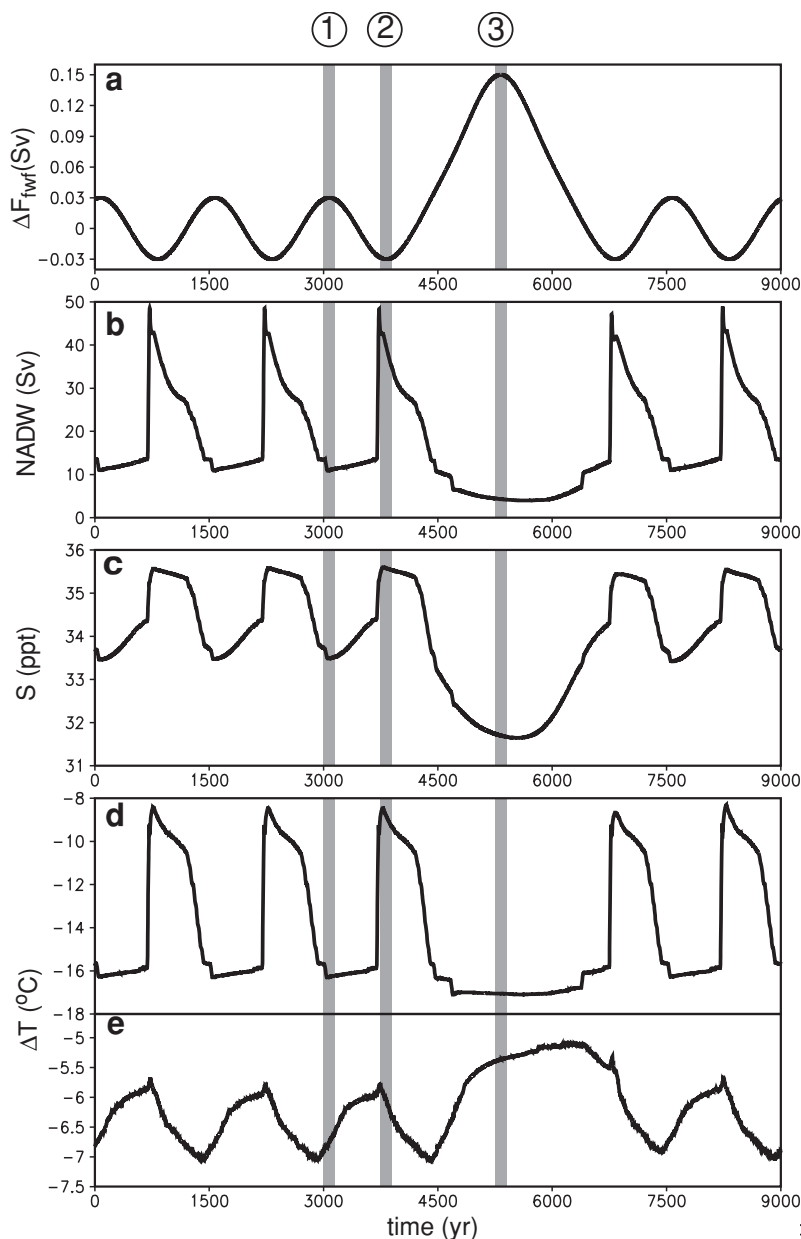


Figure 10.26 Response of the Climber-2 model, under the LGM climate to periodic freshwater forcing. (a) Freshwater forcing amplitude, (b) Atlantic MOC, (c) salinity at 60°N, (d) air temperature over the North Atlantic section and (e) air temperature over Antarctica (from Ganopolsky and Rahmstorf, 2001).

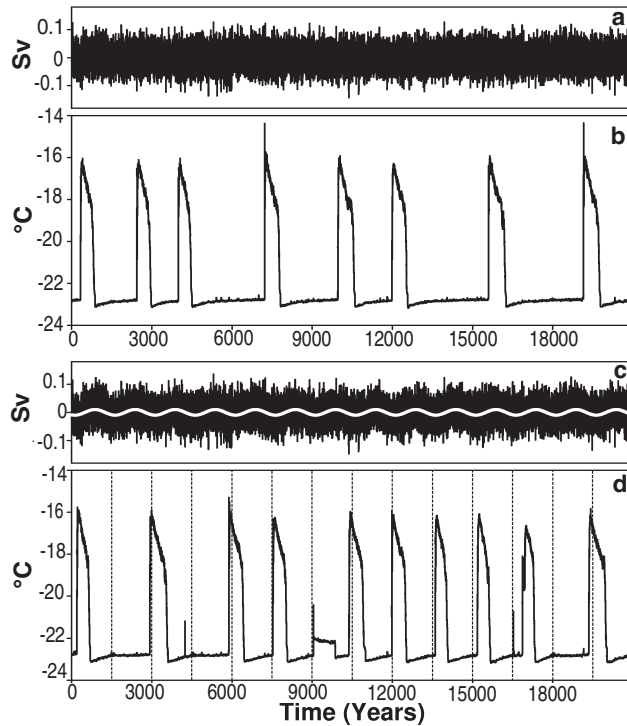


Figure 10.27 Response of the Climber-2 model to periodic freshwater forcing and noise. (a) Noisy freshwater forcing, (b) air temperature over the North Atlantic section under the forcing (a), (c) periodic plus noisy freshwater forcing and (d) air temperature over the North Atlantic section under the forcing (c) (figure from Ganopolski and Rahmstorf, 2002).

With the MOC as a central component in the mechanism, the hypotheses to explain the D-O events gather around two possibilities. The first ascribes these events to switches between equilibria or ‘excitable states’ of the MOC (Ganopolsky and Rahmstorf, 2001), where internal oscillations are not relevant, but an external periodic forcing is essential. The second involves interactions of noise with internal oscillatory behavior, which can be either loop oscillations or deep-decoupling oscillations.

The regularity of the D-O cycles in the first view results from an amplification of the periodic signal by the noise (Alley et al., 2003; Ganopolski and Rahmstorf, 2002). The waiting times between warm events in the Climber-2 model appear to show the particular features of the stochastic resonance (Fig. 10.28) and are similar to those obtained from the GRIP ice core data (Alley et al., 2003).

The immediate question, however, that arises from these results is related to the origin of the periodic forcing and, in particular, its 1,500-year time scale. The stochastic resonance theory of D-O events embraces the idea that it is related to solar forcing. Although there are no 1,500-year periodic signals known in the solar variability, there

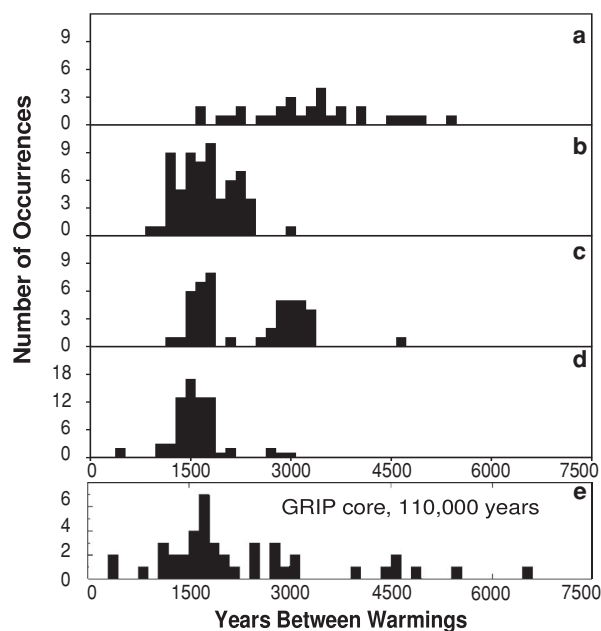


Figure 10.28 Histograms of the waiting time between warm events for ‘noise’ only situations (a,b) and for simulation with periodic forcing and noise (c,d). The standard deviation of the noise is 0.035 Sv in panels (a) and (c) and 0.05 Sv in the panels (b) and (d). Panel (e) was obtained from the GRIP ice core record (Alley et al., 2003) (figure from Ganopolski and Rahmstorf, 2002).

are the DeVries-Suess and the Gleissberg cycles, with periods of 210 and 87 years, respectively. Forcing the Climber-3 model with periodic perturbations in the freshwater flux with periodic perturbations on these frequencies can indeed provide fairly regular 1,470-year D-O events (Braun et al., 2005), even without the addition of noise (and, consequently, no stochastic resonance mechanism involved). An explanation using a conceptual model was provided in Braun et al. (2007). An open problem is, however, how such a solar forcing leads to a periodic forcing (of the same time scale) in the freshwater flux over the North Atlantic.

The second hypothesis relates the variability on millennial time scales to internal ocean modes, in particular, the overturning oscillations and the deep-decoupling oscillations. In this case, no external periodic forcing is needed, as the time scale of the variability is derived from internal instabilities. In Timmermann et al. (2003b), the coherence resonance arising through the effect of noise in the presence of a nearby limit cycle of a deep-decoupling oscillation gives rise to D-O type behaviour.

Timmermann et al. (2003b) also investigated the effect of a periodic large meltwater pulse such as associated with Heinrich events. In the presence of background noise in the freshwater flux, a Heinrich event leads to a large decrease of the MOC and a sequence of D-O events (Fig. 10.29). It is proposed that there may be a feedback

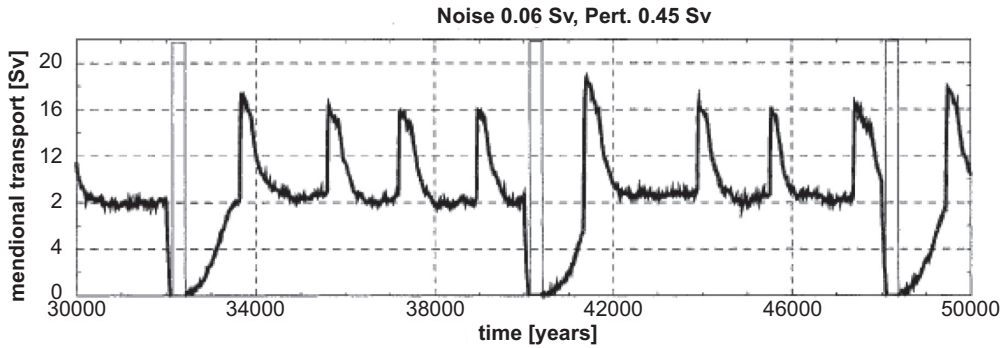


Figure 10.29 Response of the North Atlantic MOC to repeated 300-year-long meltwater pulses of 0.45 Sv in the presence of a 0.06-Sv amplitude noise forcing in the freshwater flux (figure from Timmermann et al., 2003b).

between the presence of the D-O events and the buildup of land-ice, eventually affecting the Heinrich event timing.

The coherence resonance theory, although attractive, also has problems. First, the fact that convection and vertical diffusion play a dominant role in the deep-decoupling oscillations is not very attractive, as these are elements of a climate model that are represented with minimal confidence. An oscillation mechanism based on the overturning oscillations (which are advectively controlled) would have much more preference. Second, the transition from the cold state to the excited warm state is very sensitive to parameters and is likely to be restricted to a small region in parameter space.

Coherence resonance involving the overturning oscillations has not been explored in detail. The difficulty is that the time scale of this type of oscillation depends on the spatial pattern of the MOC, being centennial for Atlantic-size basins and only millennial scale for the global ocean (Weijer and Dijkstra, 2003). In the series of studies by Sakai and Peltier (Sakai and Peltier, 1996, 1997, 1999), millennial oscillatory behaviour was found in a three-basin zonally averaged ocean model coupled to an energy-balance atmosphere model. For both the ocean-only model (Sakai and Peltier, 1996), as well as the coupled model (Sakai and Peltier, 1997), oscillatory regimes are found when the freshwater flux in the northern North Atlantic is changed. When this freshwater input exceeds a certain threshold, the dominant mode of variability appears to change from centennial scale variability into large-amplitude oscillations with millennial timescales. Unfortunately, no patterns of the MOC anomalies in the different basins are presented, and no sensitivity of the time scale to vertical diffusion is investigated. It is therefore difficult to assess which oscillation mechanism is driving the D-O type variability in these models.